

ELENA SAMSONOVA

Energy transfer probe as a tool to study
morphological and structural origins
of fluorescence quenching
in rare-earth doped nanophosphors



ELENA SAMSONOVA

Energy transfer probe as a tool to study
morphological and structural origins
of fluorescence quenching
in rare-earth doped nanophosphors

Institute of Physics, Faculty of Science and Technology, University of Tartu, Estonia.

The dissertation was admitted on 30.06.2015 in partial fulfilment of the requirements for the degree of Doctor of Philosophy in Physics, and was allowed for defense by the Council of the Institute of Physics, University of Tartu.

Supervisors: Dr. hab., PhD Yury Orlovskiy
Institute of Physics, University of Tartu, Estonia

PhD Valter Kiisk
Institute of Physics, University of Tartu, Estonia

Opponents: Prof. Dr. José García Solé,
Fluorescence Imaging Group, Faculty of Science, Universidad
Autónoma de Madrid, Spain

Dr. Valdek Mikli, Faculty of Chemical and Materials Technology,
Tallinn Technical University, Estonia

Defense: September 11, 2015 at University of Tartu, Estonia

The studies are supported by European Social Fund Mobilitas grants MTT 50, MJD 167 and FP7-PEOPLE-2-13-IRSES No 612620; the Estonian Ministry of Education and Research Project IUT2-24 and the Estonian Centre of Excellence in Research Project TK114 “Mesosystems: Theory and Applications”.



REPUBLIC OF ESTONIA
MINISTRY OF EDUCATION
AND RESEARCH

ISSN 1406-0647
ISBN 978-9949-32-895-6 (print)
ISBN 978-9949-32-896-3 (pdf)

Copyright: Elena Samsonova, 2015

University of Tartu Press
www.tyk.ee

CONTENTS

LIST OF PUBLICATIONS INCLUDED IN THE THESIS	6
Other publications	7
1. INTRODUCTION.....	8
2. THEORETICAL BACKGROUND	12
3. AIM OF THE STUDY	15
4. EXPERIMENTAL	16
4.1. Synthesis of the materials	16
4.1.1. Synthesis of the opal-phosphor nanocomposites.....	16
4.1.2. Synthesis of the Nd ³⁺ doped nanoparticles.....	17
4.2. Measurement techniques	19
4.2.1. Scanning electron microscopy	19
4.2.2. Transmission electron microscopy	19
4.2.3. Dynamic light scattering.....	19
4.2.4. Thermogravimetric analysis	19
4.2.5. X-Ray diffraction analysis.....	19
4.2.6. Infrared spectroscopy	20
4.2.7. Fluorescence spectroscopy	20
4.2.8. Fluorescence kinetics spectroscopy.....	20
5. RESULTS AND DISCUSSION	21
5.1. Energy transfer probe development.....	21
5.2. Impurity quenching kinetics of Nd ³⁺ doped nanoparticles	27
5.2.1. Energy transfer probing of Nd ³⁺ :YPO ₄ nanoparticles	28
5.2.2. Energy transfer probing of Nd ³⁺ :KYF ₄ nanoparticles	40
SUMMARY	52
SUMMARY IN ESTONIAN	54
ACKNOWLEDGEMENTS	56
EXTRA.....	57
REFERENCES.....	58
PUBLICATIONS	63
CURRICULUM VITAE	109
ELULOOKIRJELDUS.....	111

LIST OF PUBLICATIONS INCLUDED IN THE THESIS

- I. Orlovskii, Yu.V.; Basiev, T.T.; **Samsonova, E.V.**; Glushkov, N.A.; Eliseeva, S.V.; Alimov, O.K.; Orlovskii, A.Yu.; Klimonsky, S.O. Energy Transfer Probe for Characterization of Luminescent Photonic Crystals Morphology. *Journal of Luminescence*, 131(3); 2011, 449–452.
- II. Fedorenko, S.G.; Orlovskii, Yu.V., **Samsonova, E.V.** Fluctuation kinetics of the hopping fluorescence quenching in disordered solid solutions. A theoretical model and experimental evidence. *Journal of Luminescence*, 131(11); 2011, 2409–2413.
- III. **Samsonova, E.V.**; Popov, A.V.; Vanetsev, A.S.; Keevend, K.; Orlovskaya, E.O.; Kiisk, V.; Lange, S.; Joost, U.; Kaldvee, K.; Mäeorg, U.; Glushkov, N.; Ryabova, A. V.; Sildos, I.; Osiko, V.V.; Steiner, R.; Loschenov, V.B.; Orlovskii, Yu. V. An energy transfer kinetic probe for OH-quenchers in the Nd³⁺:YPO₄ nanocrystals suitable for imaging in the biological tissue transparency window. *Physical Chemistry Chemical Physics*, 16(48); 2014, 26806–26815.
- IV. Vanetsev, A.S.; **Samsonova, E.V.**; Gaitko, O.M.; Keevend, K.; Popov, A.V.; Mäeorg, U.; Mändar, H.; Sildos, I.; Orlovskii, Yu.V. Phase composition and morphology of nanoparticles of yttrium orthophosphates synthesized by microwave-hydrothermal treatment: the influence of synthetic conditions. *Journal of Alloys and Compounds*, 639; 2015, 415–421.
- V. **Samsonova, E.V.**; Popov, A.V.; Vanetsev, A.S.; Keevend, K.; Kaldvee, K.; Baranchikov, A.E.; Ryabova, A.V.; Fedorenko, S.G.; Sildos, I.; Kikas, J.; Steiner, R.; Loschenov, V.B.; Orlovskii, Y.V. Fluorescence quenching mechanism for water-dispersible Nd³⁺:KYF₄ nanoparticles synthesized by microwave-hydrothermal technique. *Journal of Luminescence*; 2015 x–x (in press).

Author's contribution

- I. Material preparation; fluorescence kinetics spectroscopy; participation in data processing; writing a part of the manuscript.
- II. Material preparation; fluorescence kinetics spectroscopy; writing a part of the manuscript.
- III. Participation in material preparation, fluorescence spectroscopy and fluorescence kinetics spectroscopy measurements; data processing, manuscript preparation.
- IV. Participation in material preparation and data discussion; writing a part of the manuscript.
- V. Participation in material preparation, fluorescence spectroscopy, fluorescence kinetics spectroscopy and DLS measurements; data processing; manuscript preparation.

Other publications

- a) Komissarova, L.N.; Ryumin, M.A.; Pukhkaya, V.V.; Samsonova, E.V.; Orlovskii, Yu.V. Synthesis and study of the properties of the $K_2Y_{1-x-y}Eu_xTb_y(MoO_4)(PO_4)$ and $K_2Y_{1-x-y}Eu_xTb_y(MoO_4)(PO_4)_{1-\delta}(VO_4)_\delta$ solid solutions. Russian Journal of Inorganic Chemistry, 56(12); 2011, 1943–1950.
- b) Orlovskii, Yu.V.; Vanetsev, A.S.; Romanishkin, I.D.; Ryabova, A.V.; Pukhov, K.K.; Baranchikov, A.E.; Samsonova, E.V.; Keevend, K.; Sildos, I.; Loschenov, V.B. Laser heating of the $Y_{1-x}Dy_xPO_4$ nanocrystals. Optical Materials Express, 5(5); 2015, 1230–1239.

I. INTRODUCTION

Unique fluorescence properties such as photostability, narrow fluorescence lines, long fluorescence lifetimes and high quantum yield make rare-earth doped nanoparticles exceptionally perspective for a variety of fields, from fluorophores and optical nanocomposites [1, 2], to solar cells [3], and, most recently, to a variety of biomedical applications [4–12].

In particular, lanthanide doped nanoparticles are widely considered to be a viable candidate for non-invasive cancer tumor imaging [7, 9, 11], if the dopant ion emits and absorbs light in the transparency window of biological tissues (700–1350 nm [11, 13]). Long fluorescence lifetimes of lanthanide ions are also advantageous in this regard: they allow one to exclude the autofluorescence of biological tissues (which is usually short-living), if time-gated detection is used. Note that this type of applications imposes on the material requirements of two types: first, biomedicine-related ones, and second, the ones associated with the material fluorescence.

To serve as a bioimaging agent, a nanoparticle colloidal solution is intended to be introduced into the human organism. The following criteria are considered to be important for a nanomaterial in this respect: low toxicity [14–16], sufficient cellular uptake and clearance rate [14, 16], and adequate immune response [14, 15]. These factors are determined by the properties of the nanomaterial and should be taken into account while selecting a suitable synthesis technique and conditions, methods of surface modification and post-synthesis treatment. Since the nanoparticles should be low-toxic, not only the nanoparticle material should be biocompatible, but also none of the potentially harmful agents should be used during the synthesis. The requirement on sufficient cellular uptake and clearance rate implies that the nanoparticles should be relatively monodisperse with the mean size less than 50 nm [16]. Considering that many natural immunologically relevant objects, including pathogens, are comparable in size with nanomaterials [17], the nanomaterial shape and surface properties should be designed in the way that does not lead to undesirable immune response upon the bioimaging agent introduction. The nanoparticle surface should be easily modifiable in order to ensure biocompatibility and provide opportunity for the particle to be targeted to a tumor [7]. Finally, as the internal medium of a human organism is aqueous, the nanoparticles should be able to form stable colloidal solutions in water [7, 18]. Note that fluorescence properties are also to some extent determined by the particle structure, i.e. by the degree of crystallinity, which imposes additional requirements on nanoparticle quality.

During the past few decades a variety of methods have been developed to synthesize rare-earth doped nanoparticles [19–40]. However, not all of the techniques allow for production of nanoparticles that meet the requirements listed above. The techniques will be further described and classified according to their applicability for synthesis of high quality nanoparticles suitable for bioimaging.

The synthesis methods applied to nanoparticle preparation may be primarily classified as following the combustion route, the gas condensation route or the wet chemical route. Although the combustion allows for obtaining highly crystalline particles, the obtained nanoparticles are usually aggregated [19], and the aggregate size distribution is usually wide. Besides, only a limited range of materials could be synthesized by this method (mainly oxide materials are synthesized by using this route, among them Y_2O_3 is the most popular for hosting rare-earth ions [19–23]). Another technique is gas-phase condensation, which implies the nanoparticle growth on a substrate [24], which cannot be separated afterwards. Some physical methods, such as laser ablation, are suitable to produce colloidal nanoparticles [25]. However, phase and composition control, as well as control over size distribution may be difficult for this technique. Therefore, only wet chemistry methods that allow for producing colloidal solutions of nanoparticles will be considered below in detail.

Among the methods suggested for the synthesis of dispersible rare-earth doped nanoparticles, thermal decomposition (or high-temperature solvolysis) technique is one of the most well-known [26–28]. It allows one to produce high quality nanoparticles with controllable size and shape and achieve good fluorescence properties. However, the synthesis is carried out in high-boiling organic media, and further dispersion of the obtained particles in water may be achieved only after complex surface modification [29–32]. This method is relatively energy-consuming. Besides, it yields toxic by-products [27], and thus its applicability for producing nanoparticles, suitable for biomedicine, is limited. Synthesis may be also carried out in polyols [33–34]. If amphiphilic surfactants are used during the synthesis, the produced nanoparticles may be redispersed in water. Under these conditions, it was reported to be suitable for the preparation of biomedical nanoparticles [34]. However, one should note that high surfactant concentration may be needed, which may be therefore harmful for a human organism.

Another group of methods include the ones suitable for producing hydrophilic nanoparticles, which are easily dispersible in aqueous medium without further surface modification. For example, the microemulsion technique [35–37] has been suggested for synthesis of nanoparticles dispersible in water, as well as in organic solvents, depending on whether direct or inverse micelles are formed. This method allows one to control the nanoparticle size and size distribution. However, large amounts of surfactants are usually needed, which may be unsuitable for further biomedical applications. Besides, the reaction yield is relatively low [35]. The co-precipitation [35, 38] and sol-gel [35] techniques are easy to conduct and environmentally benign, and the reaction yield associated with them is much higher, but the size distribution of the resulting nanoparticles is often wide. Moreover, the nanoparticle crystallinity is relatively low, and thus thermal post-treatment is needed. Unfortunately, along with better crystallinity, the high-temperature treatment leads to the nanoparticle aggregation. Synthesis in hydrothermal conditions [35, 39] allows one to

overcome this drawback, since the resulting nanoparticles are well-crystalline and at the same time highly water-dispersible. Note that this technique requires the use of an autoclave, and is relatively time and energy demanding. The latter issue may be solved by using microwave radiation instead of a conventional energy source [40].

Apart from high biocompatibility and other biomedicine-related properties, bioimaging also requires the nanomaterial to demonstrate high brightness even in low concentration colloidal solutions, and thus high fluorescence quantum yield. The main problem to overcome in this respect is nonradiative quenching competing with the radiative relaxation. It may take place in rare-earth doped materials and substantially decrease the efficiency of the desirable photon emission. For the non-radiative energy transfer to be possible, apart from the emitting ions, which serve as energy donors, there should be ions or functional groups, which may accept energy. In general, energy may be transferred between alike or different centers, and the main requirement for energy transfer to take place is the presence of the resonant or close to resonance energy transitions in the donor and acceptor. For this the spectral lines in the emission spectrum of the donor have to overlap substantially with some absorption lines of the acceptor. Phonon emission or absorption compensates for energy mismatch between two energy transitions, the one in donor and the one in the acceptor [41].

Initially, the theory of static fluorescence quenching was developed for quenching by other impurity ions and self-quenching in bulk crystals [42, 43]. The quenching causes optical excitation energy loss (and thus a decrease in the fluorescence quantum yield). This theory was further applied to such processes as fluorescence quenching by $-OH$ groups, which can be observed in the disordered media, for example, in glasses [44]. Note that at high donor concentrations fluorescence quenching is no more static, as energy migration over the donor ions starts affecting it.

Although water-based techniques are generally more preferable for synthesis of biomedicine-related nanomaterials, as shown above, in nanoparticles, synthesized in water, a large number of defects (including $-OH$ groups) is usually observed, which can serve as energy acceptors. On the one hand, it results in a significant reduction of the fluorescence quantum yield in comparison with bulk crystals. On the other hand, even though fluorescence quenching is usually considered non-desirable, one may use it as a diagnostic tool to study the structural and morphological origins of the fluorescence quenching in the material.

Energy transfer probe has been shown to be an effective tool for assessment of the distances in the biomolecules [45] and of the dimensionality of the acceptor space [46], which are related to the material structure and morphology. In the framework of this thesis the approach was further developed to reveal the dimensionality of the space where acceptors are distributed in the fluorescent opal structures and to evaluate the spatial distribution of the energy acceptors in $Nd^{3+}:YPO_4$ and $Nd^{3+}:KYF_4$ nanoparticles, which are intended to be potential

agents for fluorescent bioimaging. Note that the matrices with large intercationic distances were chosen to reduce the effect of self-quenching. We found that in the case of the fluorescent opals the acceptor space is 2-dimensional, and in the case of the nanoparticles it is 3-dimensional. This allows us to make conclusions regarding the material morphology and structure. Thus, we showed that fluorescence acceptors in the nanoparticles are mainly distributed in the material volume, not on the surface of the nanoparticles. Along with this, we evaluated and compared quenching parameters for different materials.

2. THEORETICAL BACKGROUND

As it was mentioned in the previous chapter, lanthanide doped materials have a wide variety of potential applications because of their good luminescent properties, i.e. high fluorescence quantum yield. However, the fluorescence quantum yield may be significantly decreased due to the fluorescence quenching effects. It is observed in a wide range of solid state materials. In highly ordered systems like laser single crystals both donors and acceptors are represented by lanthanide ions, either of the same type or different types. In glasses, energy transfer caused by vibrations of $-OH$ molecular groups inevitably present in the systems also leads to fluorescence quenching.

In general, energy transfer (or impurity quenching) kinetics is a complex process that consists of several stages depending on the donor and acceptor concentrations. At vanishingly small concentrations of donors, the excitation cannot migrate over donor ions and therefore dies (in other words, is quenched) at the place of origin. In this case the impurity quenching is referred to as static. In general, it may be described by two subsequent stages. During the initial, so-called ordered stage, the excitations are mainly quenched by acceptors positioned in the nearest coordination spheres of a donor. In this stage the quenching kinetics is exponential [43]:

$$N_{\text{ord.}}(t) = \exp(-W_0 t), \quad (1)$$

with its rate described as:

$$W_0 = c_A C_{DA} \sum_{i=1}^N R_i^{-s}, \quad (2)$$

where c_A is the relative acceptor concentration, $\sum_{i=1}^N R_i^{-s}$ is the lattice sum over all the acceptors sites, s is the multipolarity of the donor-acceptor interaction, and C_{DA} is a microparameter of the donor-acceptor interaction. The latter is defined through:

$$W_{DA} = C_{DA}/r^s, \quad (3)$$

where W_{DA} is the donor-to-acceptor energy transfer rate, and r is the distance between the donor and the acceptor.

Note that for dipole-dipole interactions, which will be mainly considered below, $s = 6$ [42].

After this stage, the second stage of the static quenching starts, namely, the nonexponential disordered stage. For the case of uniform and equiprobable distribution of acceptors in the space of arbitrary dimension D the averaging over the rates of the individual donor-acceptor interactions yields the Förster-type stage [46]:

$$N(t) = \exp(-\gamma_A t^{D/s}), \quad (4)$$

where γ_A is the macroparameter of donor-acceptor interactions, which is for arbitrary multipolarity and acceptor space dimension defined as:

$$\gamma_A = V_D \Gamma(1 - D/s) n_A C_{DA}^{D/s}, \quad (5)$$

where n_A is the average acceptor concentration per unit volume of space and Γ is the gamma function. The factor V_D depends on the acceptor space dimension: for $D = 1$, $V_D = 2$; for $D = 2$, $V_D = \pi$; and for $D = 3$, $V_D = 4\pi/3$ [46].

In the case of dipole-dipole donor-acceptor interactions and $D = 3$, which is often realized in the rare-earth doped luminescent materials, this yields a well-known equation [42]:

$$\gamma_A = (4/3)\pi^{3/2}(n_A \sqrt{C_{DA}}) \quad (6)$$

As the concentration of donors increases, migration of energy over donors to acceptors starts accelerating the quenching, and the impurity quenching kinetics becomes more complex.

In general, two different mechanisms are possible for the excitation delocalization over a system of homogeneously distributed donors. To distinguish between them one needs to consider the so-called black sphere model [47]. If the radius of a so-called black sphere where excitation is quenched, is large, the excitation delocalization may be described as continuous diffusion. Otherwise, the excitation is transferred into the black sphere at once, and the corresponding quenching mechanism is called hopping. In the limiting case of ultrafast migration the distinction is blurred [48].

The limits of the applicability of the diffusion and hopping model are defined by the relationship between C_{DA} (the microparameter of the donor-acceptor interaction) and C_{DD} (the microparameter of the donor-donor interaction, defined through $W_{DD} = C_{DD}/r^6$, where W_{DD} is the donor-to-donor energy transfer rate, and r is the distance between two donors), proportional to the probabilities of the corresponding energy transfer processes. For instance, for rare-earth containing glasses [44] the quenching of the fluorescence of rare-earth ions by vibrations of $-OH$ groups is accelerated by energy migration over the rare-earth ions, $C_{DD} \gg C_{DA}$, and thus quenching is hopping. In the following sections, this mechanism will be considered.

For hopping quenching, two additional stages of the impurity quenching kinetics may arise after static quenching is over. The first one is a well-known quasi-stationary migration accelerated stage, or a migration accelerated stage with a constant rate, at which quenching in regions rich in donors occurs. The second one is the fluctuation stage [49], related to quenching in regions depleted of donors. The interplay between the two stages is governed by the parameter α , which in the case of dipole-dipole interactions between the donor and acceptor and between the donors is defined as [49–51]:

$$\alpha = \frac{n_A \sqrt{C_{DA}}}{n_D \sqrt{C_{DD}}}, \quad (7)$$

where C_{DD} is the microparameter of donor-donor interactions and n_D is the acceptors concentration per space unit.

As shown above, for hopping mechanism $C_{DA}/C_{DD} \ll 1$, so the concentration ratio n_A/n_D plays a decisive role in the presence of each stage. Let us consider the case when the contribution of self-quenching is negligibly small (to the best of our knowledge, no theoretical approach has been suggested to date to describe migration accelerated quenching in systems with many types of acceptors). When $n_A \approx n_D$, $\alpha \ll 1$, static quenching is followed by a transitional region, after which the quasi-stationary migration-accelerated stage [52] is observed:

$$N_{bin}(t) = (1 - 2\alpha) \exp(-\bar{W}_{bin}t) \approx e^{-2\alpha - \bar{W}_{bin}t}, \quad (8)$$

the rate of which is described as:

$$\bar{W}_{bin} = \frac{\gamma_A \gamma_D}{2} \quad (9)$$

On the contrary, when the concentration of acceptors (other than donors) is significantly higher than the donor concentration, α is large (α is close to, or greater than 1), the so-called fluctuation stage may be observed in the corresponding time range [49-51]:

$$\frac{4(1 + \alpha)^2}{(\gamma_A + \gamma_D)^2} = t_s \ll t \ll t_f = \frac{4}{\alpha^2(\gamma_A + \gamma_D)^2} \quad (10)$$

This stage is similar to the static one, but the decrement is greater [49–51]:

$$N_f(t) = \left[\frac{1 + \alpha}{\alpha} \right] \exp(-(\gamma_A + \gamma_D)\sqrt{t}), \quad (11)$$

where γ_D is the macroparameter of donor-donor interactions, which in the case of dipole-dipole interactions between the donors and $D = 3$ is defined as:

$$\gamma_D = (4/3)\pi^{3/2}(n_D\sqrt{C_{DD}}) \quad (12)$$

Note that this stage may be observed either after the quasi-stationary one (which in the case is limited by t_s), or immediately after the static stage, if the acceptor concentration is extremely high [50, 51].

As may be seen from Eqs. (6, 12), one can alternatively write for α [50, 51]:

$$\alpha = \gamma_A/\gamma_D \quad (13)$$

To sum up, the fluorescence quenching is static in the case of vanishingly small donor concentrations and migration accelerated in the case of higher donor concentrations. Through a careful analysis of the impurity quenching kinetics, one can reveal the quenching mechanism, calculate the dimensionality of the donor and acceptor spaces, and draw a conclusion on structural and morphological origins of quenching.

3. AIM OF THE STUDY

The main goal of the thesis was to study the fluorescence properties of Nd^{3+} doped crystalline nanoparticles in order to obtain new information about the structural and morphological origins of the fluorescence quenching in these materials. To achieve this, the following specific objectives were pursued:

- 1) To obtain monodisperse and highly water-dispersible Nd^{3+} doped nanoparticles, which are able to form suspensions of individual particles, by means of the microwave-hydrothermal synthesis technique.
- 2) To develop the energy transfer probing technique based on the study of fluorescence quenching kinetics of the nanomaterials using $\text{Tb}_x\text{Y}_{1-x}(\text{pyca})_3 \cdot n\text{H}_2\text{O}$ chelate complexes in opal-phosphor nanocomposites and powders as model objects.
- 3) To establish a link between the fluorescence properties of the material and its structure and morphology using this tool.
- 4) To study fluorescence kinetics properties of the Nd^{3+} doped nanoparticles in order to reveal the fluorescence quenching mechanisms.
- 5) To compare the fluorescence quenching mechanisms in the nanoparticles with those in bulk crystals.

4. EXPERIMENTAL

4.1. Synthesis of the materials

In the framework of this study two types of materials were synthesized. First, opal-phosphor nanocomposites based on the rare-earth complexes with 2-pyrazinecarboxylic acid, which are embedded into silica inverse opal templates. Second, $\text{Nd}^{3+}:\text{YPO}_4$ and $\text{Nd}^{3+}:\text{KYF}_4$ nanoparticles with different dopant concentrations.

4.1.1. Synthesis of the opal-phosphor nanocomposites

4.1.1.1. Synthesis of the phosphor

As starting compounds for the synthesis of chelate complexes $\text{Tb}(\text{pyca})_3 \cdot n\text{H}_2\text{O}$ and $\text{Tb}_{0.01}\text{Y}_{0.99}(\text{pyca})_3 \cdot n\text{H}_2\text{O}$ the following reagents were used: 2-pyrazinecarboxylic acid (Aldrich, 99%), high purity $\text{Tb}(\text{NO}_3)_3 \cdot 6\text{H}_2\text{O}$ (Aldrich, 99.999%), high purity $\text{Y}(\text{NO}_3)_3 \cdot 4\text{H}_2\text{O}$ (Aldrich, 99.999%), ammonium hydroxide aqueous solution (25%). The Tb chelate complex with 2-pyrazinecarboxylic acid was synthesized according to the procedure described in [53]. In brief, at the first stage of the synthesis the Tb hydroxide is obtained by precipitation using the aqueous ammonium hydroxide solution.

2-pyrazinecarboxylic acid taken with 10% excess is then added to the freshly precipitated hydroxide form $\text{Tb}(\text{pyca})_3 \cdot n\text{H}_2\text{O}$ at room temperature. The $\text{Tb}_{0.01}\text{Y}_{0.99}(\text{pyca})_3 \cdot n\text{H}_2\text{O}$ complex was prepared in the similar way with $\text{Tb}(\text{NO}_3)_3 \cdot 6\text{H}_2\text{O}$ partially replaced by $\text{Y}(\text{NO}_3)_3 \cdot 4\text{H}_2\text{O}$. The samples were dried under vacuum at 80°C for 20 min. The complex compositions were confirmed by thermogravimetric analysis, infrared spectroscopy and elemental analysis.

4.1.1.2. Synthesis of the inverse opal template

a) Synthesis of the polystyrene microspheres

To synthesize the monodisperse polystyrene microspheres styrene (Aldrich, >99%, with 4-tert-butylcatechol as a stabilizer) was used as a starting reagent. To remove the stabilizer, styrene was distilled under vacuum. The polystyrene microspheres were obtained by means of emulsifier-free heterogeneous polymerization of styrene using potassium persulfate as a polymerization initiator according to the procedure described in [54]. The mixture of 450 ml of distilled water, 30 ml of styrene, and 0.415 g of $\text{K}_2\text{S}_2\text{O}_8$ was kept under vigorous stirring for 24 hours at 70°C .

b) Synthesis of the polystyrene based opal template

The polystyrene based opal templates were synthesized as described in [55] by self-assembly of the microspheres onto the vertical glass slides, which had been thoroughly cleaned and then immersed into 1 vol.% aqueous suspension of the

microspheres. The system was left undisturbed at 50°C for 24 hours allowing the solvent to evaporate slowly and the opal-like structure to be formed at the solid/liquid/gas interface.

c) Opal inversion

To obtain the inverse opal template as described in [56], tetraethoxysilane (Aldrich, >99%) was used as a precursor. The lower edge of a pre-prepared opal film was immersed vertically into the reaction mixture containing tetraethoxysilane (6 ml), water (3 ml), concentrated hydrochloric acid (1 ml) and ethanol (4 ml), so that the voids of the opal structure could be filled with the solution due to capillary forces. The samples were left in air for tetraethoxysilane hydrolysis. Calcination at 550°C for 10 hours following slow heating (heating rate 1°C/min) led to the formation of a porous silica inverse opal template.

4.1.1.3. Synthesis of the opal-phosphor nanocomposites

To obtain the opal-phosphor nanocomposites, the silica-based inverse opal films were soaked with the phosphor water-ethanol solutions as described in [57] and then dried under vacuum at 80°C for 20 min.

4.1.2. Synthesis of the Nd³⁺ doped nanoparticles

Nd³⁺:YPO₄ and Nd³⁺:KYF₄ nanoparticles were synthesized by means of the microwave-hydrothermal technique. As it was pointed above, hydrothermal conditions allow one to obtain better crystallinity in comparison with that obtained via the common precipitation technique. At the same time, microwave heating makes the treatment procedure more time and energy efficient in comparison with hydrothermal synthesis under conventional heating.

4.1.2.1. Synthesis of Nd³⁺:YPO₄ nanoparticles

In the course of the preparation of the Nd³⁺:YPO₄ nanoparticles the commercially available Nd(NO₃)₃·5H₂O (Aldrich, 99.999% purity), Y(NO₃)₃·4H₂O (Aldrich, 99.999% purity), and K₂HPO₄·3H₂O (Aldrich, 99.9% purity) were used as precursors without additional purification or analysis. The synthesis methods are described in detail in [III, IV].

First, the solutions of Y(NO₃)₃·4H₂O and Nd(NO₃)₃·5H₂O in deionized water were prepared, with their concentrations depending on the aimed doping level in the nanoparticles (5 mmol of Y(NO₃)₃·4H₂O for pure yttrium phosphate nanoparticles, 4.950 mmol of Y(NO₃)₃·4H₂O and 0.050 mmol of Nd(NO₃)₃·5H₂O in 10 ml of water for 1 at.% of Nd³⁺; 4.995 mmol of Y(NO₃)₃·4H₂O and 0.005 mmol of Nd(NO₃)₃·5H₂O in 10 ml of water for 0.1 at.% of Nd³⁺). The solutions

were added dropwise to the preliminary prepared 5 mmol solution of $\text{K}_2\text{HPO}_4 \cdot 3\text{H}_2\text{O}$ in 30 ml of deionized water under stirring, then left under stirring for 15 min. The freshly precipitated gels were diluted in the mother solution with 10 ml of deionized water, and then exposed to the microwave-hydrothermal treatment using the Berghof Speedwave-3M+ (Germany) laboratory device. As it was shown in [IV], the microwave-hydrothermal treatment at 200°C for two 2 hours was sufficient to obtain well-crystalline nanoparticles of about 40 nm in size. The samples were then collected, centrifuged, washed several times with deionized water and air-dried for 2 hours at 50°C . For optical measurements, they were further dried for 10 hours at 200°C

To eliminate most of the $-\text{OH}$ groups positioned on the outer surface of the nanoparticles as well as the ones distributed in their volume (e.g. in the mesopores in the form of molecular water), and thus reduce fluorescence quenching, two options were used. First, one sample of the 0.1 at.% $\text{Nd}^{3+}:\text{YPO}_4$ nanoparticles was annealed at 900°C for 5 hours. As it will be shown below, such treatment had a great impact on the material fluorescence properties, but also led to irreversible nanoparticle aggregation. Second, a part of the $\text{Nd}^{3+}:\text{YPO}_4$ nanoparticles was prepared using heavy water (deuterium oxide, Aldrich, 99.9%) instead of deionized water to prepare all the solutions. After drying the samples were stored in a dessicator.

4.1.2.2. Synthesis of $\text{Nd}^{3+}:\text{KYF}_4$ nanoparticles

As starting compounds for the preparation of the nanoparticles of the cubic modification of $\text{Nd}^{3+}:\text{KYF}_4$ $\text{Y}(\text{NO}_3)_3 \cdot 4\text{H}_2\text{O}$ (Aldrich, 99.999% purity), $\text{Nd}(\text{NO}_3)_3 \cdot 5\text{H}_2\text{O}$ (Aldrich, 99.999% purity), KF (Aldrich, >99% purity), and D_2O (Aldrich, 99.9%) were used. The synthesis was carried out according to the similar procedure, using solutions of $\text{Y}(\text{NO}_3)_3 \cdot 4\text{H}_2\text{O}$ (4.950 mmols or 4.995 mmols in 10 ml of deionized water) and $\text{Nd}(\text{NO}_3)_3 \cdot 5\text{H}_2\text{O}$ (0.050 or 0.005 mmol in 10 ml of deionized water) or D_2O for 0.1 at.% and 1 at.% $\text{Nd}^{3+}:\text{KYF}_4$, respectively, as well as the solution of 50 mmols of KF in 30 ml of deionized water or deuterium oxide. Since high dispersibility in aqueous medium is required for materials intended for biomedical applications, Emuksol-268 (NIOPIK), a biocompatible poloxamer, was added either to the mixture of solutions of rare-earth nitrates before the gel precipitation (sample 1) or to the freshly precipitated gel before the microwave-hydrothermal treatment (sample 2) in order to improve the dispersibility of the resulting nanoparticles. The microwave-hydrothermal treatment was conducted at 200°C for 4 hours. The samples were collected, centrifuged, washed several times with deionized water and air-dried for 2 hours at 50°C . For optical measurements, they were further dried for 2 hours at 100°C .

4.2. Measurement techniques

The experimental techniques applied for characterization of the materials are described in more detail in the corresponding publications. Here only brief description will be given.

4.2.1. Scanning electron microscopy

The morphology of opal-phosphor nanocomposites was studied using a FEI Quanta 600 (USA) microscope at low vacuum, at 15 kV accelerating voltage.

4.2.2. Transmission electron microscopy

The morphology of the nanoparticles was studied by means of a Leo912 AB Omega (Germany) electron microscope and a Tecnai 10 (USA) electron microscope at 100 kV accelerating voltage.

4.2.3. Dynamic light scattering

Water dispersibility of the nanoparticles was studied by means of the dynamic light scattering technique using a Photocor Complex spectrometer. For the measurements water colloids with the concentration of the nanoparticles of 0.1 mg/mL were prepared and intensively ultrasonicated for 1 min using a Bandelin SONOPLUS HD2070 with a submersible waveguide KE76. In the case of $\text{Nd}^{3+}:\text{YPO}_4$ nanoparticles different surfactants were used while obtaining the colloids to improve the nanoparticle dispersibility. The procedure for the colloid preparation is described in detail in [V].

4.2.4. Thermogravimetric analysis

TGA/DTA experiments were carried out using a LABSYS evo 1600 thermoanalyzer coupled to a Pfeiffer mass spectrometer by a heated transfer line, allowing for the analysis of effluent gases.

4.2.5. X-Ray diffraction analysis

The X-ray diffraction analysis of the nanoparticles was performed by means of a D/MAX 2500 diffractometer and a SmartLab diffractometer (Rigaku, CuK_α -radiation). We identified diffraction peaks using the JCPDS database and [58, 59].

4.2.6. Infrared spectroscopy

Infrared absorption spectroscopic analysis was carried out using a Perkin Elmer Spectrum GX FT-IR spectrometer.

4.2.7. Fluorescence spectroscopy

Fluorescence spectra of the opal-phosphor nanocomposites were measured using a Perkin Elmer LS 55 (USA) fluorescence spectrometer at $\lambda_{ex} = 337$ nm. The fluorescence excitation and emission spectra of the nanoparticles were recorded either by means of a HORIBA Fluoromax-4 spectrofluorometer or by using the setup described below. Both setups allowed measurements conducted at room temperature or at 10 K, if using an Utreks-type helium-bath optical cryostat.

4.2.8. Fluorescence kinetics spectroscopy

The Tb³⁺ fluorescence kinetics in the opal-phosphor nanocomposites was detected as described in [I] after the excitation of the ligand, which acts as a sensitizer, by means of a nitrogen laser at 337 nm (pulse duration 2 ns, repetition rate 10–200 Hz). The fluorescence was dispersed by an MDR-23 monochromator (LOMO) and detected in the visible spectral range at room temperature using a R636-10 photomultiplier (Hamamatsu). The scattered light of the laser excitation was suppressed by means of a color filter NS-6 (USSR, Mashpriborintorg). The fluorescence kinetics curves were recorded at impedances of 300 Ω , 1 k Ω , 10 k Ω , 30 k Ω , and 100 k Ω , coupled to the input of a TDS 3032B oscilloscope (DC Series, Tektronix) with up to 350 MHz bandwidth, so that the partial saturation at large impedances was obtained.

The parts of the measured curves with best signal-to-noise ratio and appropriate time resolution were normalized to a curve measured at the lowest impedance and combined to a single curve. This technique allowed for a substantial increase of the dynamic range of the measurements.

The fluorescence kinetics and a part of the fluorescence emission spectra of the nanoparticles were measured as described in the [III, V] at room temperature in the NIR spectral range after a pulsed excitation from an optical parametric oscillator (OPO) Ekspla NT342/1/UVF (measured pulse duration 15 ns, repetition rate 20 Hz). The fluorescence was dispersed by an MDR-23 monochromator (LOMO) and detected by a Pheu-79 photomultiplier in the photon counting mode using a Fast ComTec P7882 multi-channel analyzer (time resolution 100 ns). The scattered light of the laser excitation was suppressed by means of an edge-filter BLP-785R (Semrock) placed in front of the entrance slit of the monochromator.

5. RESULTS AND DISCUSSION

5.1. Energy transfer probe development

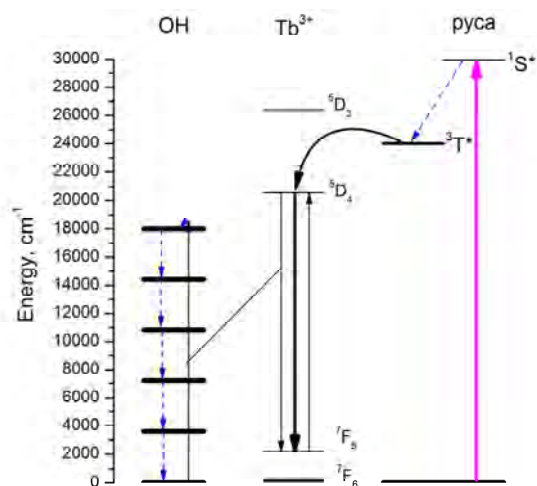
Fluorescence quenching is generally an undesirable process leading to the decrease of the fluorescence quantum yield in the material. However, the impurity quenching causes identifiable peculiarities in the fluorescence decay kinetics, which may serve as a diagnostic tool for elucidating the morphological and structural origins of the fluorescence quenching. As a model object for the development of the kinetics analysis $[Y_{0.99}Tb_{0.01}(pyca)_3(H_2O)_2] \cdot nH_2O$ and $[Tb(pyca)_3(H_2O)_2] \cdot nH_2O$ chelate complexes were chosen, each in two modifications: either as a complex powder, or a film formed on the surface of the voids of silica-based inverse opal. The kinetics analysis procedure is essentially different for the two complexes. Low dopant concentration does not allow for significant energy migration over Tb^{3+} ions (which is inevitable for the pure Tb^{3+} complex), so only static quenching by $-OH$ acceptors takes place (Fig. 1). In this chapter, first, the simpler case of the $[Y_{0.99}Tb_{0.01}(pyca)_3(H_2O)_2] \cdot nH_2O$ complex will be considered, which will be further compared with the more complicated case of $[Tb(pyca)_3(H_2O)_2] \cdot nH_2O$ complex.

Prior to fluorescence measurements, the samples of the $Tb(pyca)_3 \cdot nH_2O$ and $Tb_{0.01}Y_{0.99}(pyca)_3 \cdot nH_2O$ complexes and the opal-phosphor nanocomposites based on the complexes were dried in vacuum ($80^\circ C$, 30 min) in order to stabilize the hydrate composition of the complexes. The fluorescence spectrum of the $Tb(pyca)_3 \cdot nH_2O$ complex after the vacuum drying, which was measured after the excitation at 337 nm, shows relatively high fluorescence intensity and well-pronounced maxima, corresponding to the $^5D_4 - ^7F_j$ ($j = 0 - 6$) transitions of the Tb^{3+} ion (Fig. 2). The most intensive maximum corresponds to the $^5D_4 - ^7F_5$ transitions, at which the fluorescence kinetics was detected.

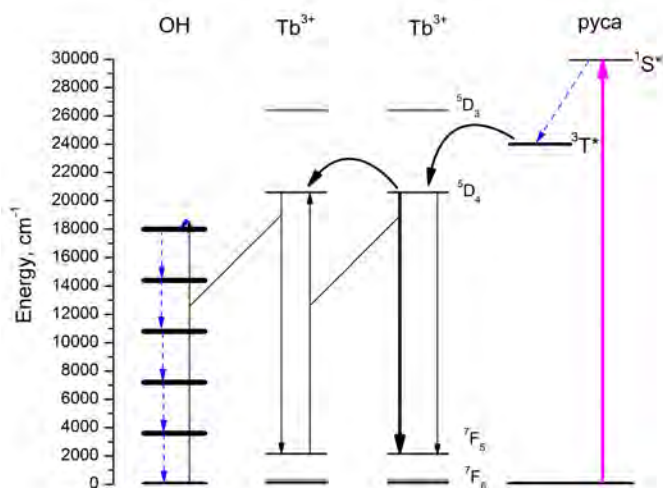
The kinetics of impurity quenching $N(t)$ may be obtained in accordance with the following equation:

$$I_{meas}(t) = N(t) \exp(-t / \tau_R), \quad (14)$$

where $I_{meas}(t)$ is the measured fluorescence kinetics (normalized to unity); and τ_R is the fluorescence radiative lifetime.



a)



b)

Fig. 1. The scheme of excitation and relaxation of the 5D_4 level of the Tb^{3+} ion in the chelate organic complexes with 2-pyrazinecarboxylic acid (based on [53]). The initial excitation of the singlet state of the (pyca) ligand is followed by non-radiative relaxation to the triplet state of the (pyca) ligand, and finally transferred to the 5D_4 level of the Tb^{3+} ion. Red arrow – laser excitation, thick black arrow – luminescence, arc arrows – energy transfer, thin black arrows – cross-relaxational transitions which govern nonradiative energy transfer, dashed arrows – multiphonon relaxation. Quenching is caused by $-OH$ vibrations (a) and may be accelerated by migration of energy over donors to acceptors in the case of high donor concentrations.

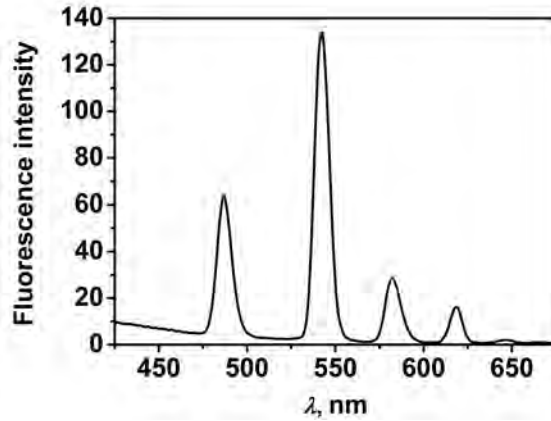


Fig. 2. The fluorescence spectrum of the $\text{Tb}(\text{pyca})_3 \cdot n\text{H}_2\text{O}$ complex, $\lambda_{ex} = 337 \text{ nm}$.

In the case of the radiative decay the fluorescence radiative lifetime could be directly found from the slope of the kinetics curve. However, the fluorescence kinetics curves for the $[\text{Y}_{0.99}\text{Tb}_{0.01}(\text{pyca})_3(\text{H}_2\text{O})_2] \cdot n\text{H}_2\text{O}$ complex as powders, as well as films in the voids of inverse opal structures, are nonexponential (Fig. 3), so processes other than radiative decay are present. In the case of the low Tb^{3+} concentration this behavior may be explained by energy transfer from the $^5\text{D}_4$ emitting level of Tb^{3+} ions to vibrational levels of $-\text{OH}$ groups with subsequent non-radiative relaxation, since the lanthanide complexes with 2-pyrazinecarboxylic acid are known to form hydrates with variable water content [53]. As mentioned above, for Tb^{3+} complex the situation is even more complex, since for such a high dopant concentration quenching is accelerated by energy migration over Tb^{3+} ions to $-\text{OH}$ groups (this case will be considered further). However, one may estimate the fluorescence radiative lifetime for the powder of the kinetics curve obtained for the $[\text{Y}_{0.99}\text{Tb}_{0.01}(\text{pyca})_3(\text{H}_2\text{O})_2] \cdot n\text{H}_2\text{O}$ complex powder, which is plotted as $\ln(I_{meas})$ vs. t , since the last stage of the kinetics is exponential. The approximate value $\tau_R = 1.94 \text{ ms}$ was obtained.

As it was mentioned above, for the low Tb^{3+} concentration energy migration over donors to acceptors is insignificant; and the late Förster stage of the energy transfer kinetics may be described by Eqs. (4, 5). Therefore, from the slope of the kinetics curve plotted as $-\lg(-\ln(N(t)))$ vs. $\lg t$ (Fig. 4) one can assess the slope, equal to the D/s ratio (Eq. (4)). $D/s = 1/2$ for the powders of the complexes, and $D/s = 1/3$ for the films in the voids of the inverse opals (Fig. 4). Since the contribution of the quadrupole transitions for Tb^{3+} ions is insignificant in comparison with that of dipole transitions [60], the donor-acceptor interactions may be considered as dipole-dipole, and thus $s = 6$ in Eq. (4). Therefore, one can calculate $D = 3$ for the powder of the complex, and $D = 2$ for the film of the complex. This means that in the case of the powder of the complex acceptors are uniformly and equiprobably distributed in the volume of

the material, similarly to the case of the glasses, and are likely represented by the –OH groups of the crystalline water molecules. In contrast, in the case of the film of the complex the –OH acceptors are distributed on the surface. It is well known that the surface of silica is covered with a large number of –OH groups, which are presumably the main source of the fluorescence quenching in this case. Therefore, these two cases can be easily distinguished using the energy transfer probing technique, based on the analysis of the impurity quenching kinetics.

This trend may be confirmed by plotting the impurity quenching kinetics as $\ln(N(t))$ vs. $t^{D/s}$ (Fig. 5). The kinetics curve for the $[Y_{0.99}Tb_{0.01}(pyca)_3(H_2O)_2] \cdot nH_2O$ embedded into the inverse opal template is linearized when represented as $\ln(N(t))$ vs. $t^{1/3}$ (Fig. 5a), which again reveals the 2-dimensional distribution of acceptors. The slope of the curve in this representation corresponds to the γ_A macroparameter, so $\gamma_A = 20.3 \text{ s}^{-1/3}$. Likewise, the kinetics curve of the powder of the same complex is linearized when represented as $\ln(N(t))$ vs. $t^{1/2}$ (Fig. 5b), and the $\gamma_A = 35.6 \text{ s}^{-1/2}$ [I] may be found using the same technique (the latter value was further refined to be $\gamma_A = 34 \text{ s}^{-1/2}$) [II].

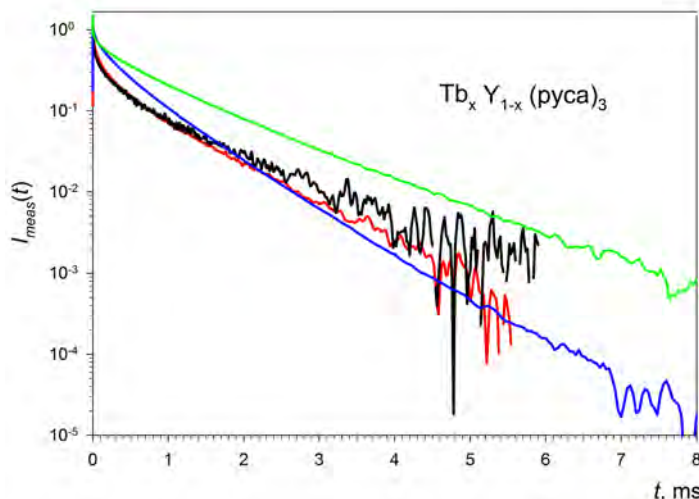


Fig. 3. Fluorescence kinetics decay of chelated complexes with 2-pyrazinecarboxylic acid: $[Y_{0.99}Tb_{0.01}(pyca)_3(H_2O)_2] \cdot nH_2O$ in the inverse SiO_2 opal template voids (black line); 2 – $[Tb(pyca)_3(H_2O)_2] \cdot nH_2O$ in the inverse SiO_2 opal template voids (red line); the powder of $[Y_{0.99}Tb_{0.01}(pyca)_3(H_2O)_2] \cdot nH_2O$ (green line); and the powder of $[Tb(pyca)_3(H_2O)_2] \cdot nH_2O$ (blue line). The kinetics were measured at room temperature under 337 nm excitation and 544 nm fluorescence detection – solid lines. (Adapted from [I].)

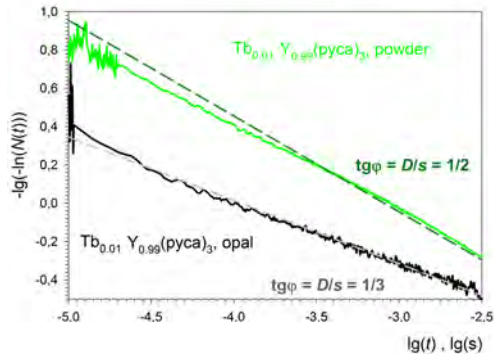


Fig. 4. Energy transfer kinetics of the powder of $[Y_{0.99}Tb_{0.01}(pyca)_3(H_2O)_2] \cdot nH_2O$ complex (green line) and $[Y_{0.99}Tb_{0.01}(pyca)_3(H_2O)_2] \cdot nH_2O$ in the inverse opal template voids (black line) represented as: (a) $-\lg(-\ln(N(t)))$ vs. $\lg t$, and (b) $\ln(N(t))$ vs. $t^{1/2}$. Dashed lines represent the linear fitting with the slope of $1/3$ (gray line) and (b) the slope of $1/2$ (dark green line). (Adapted from [I].)

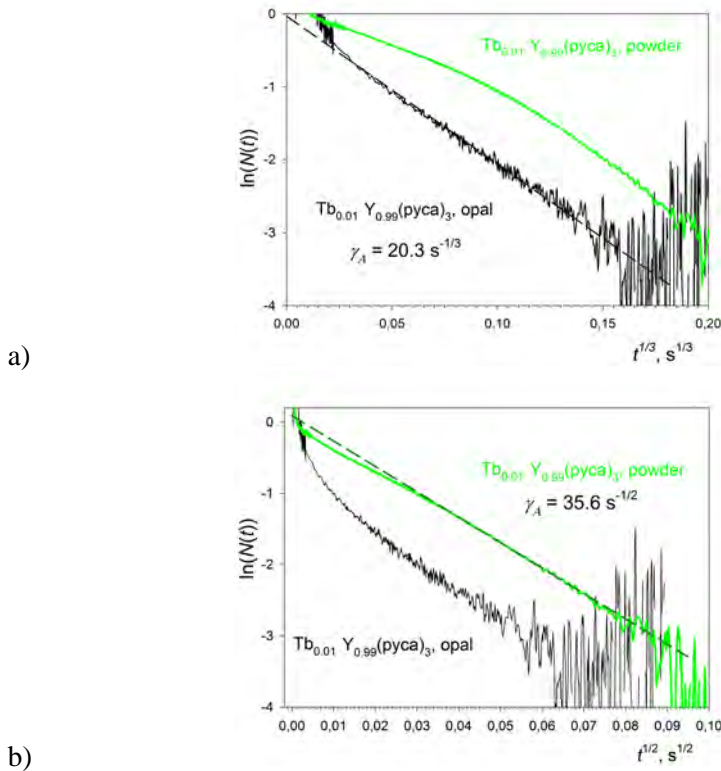


Fig. 5. Energy transfer kinetics of the powder of $[Y_{0.99}Tb_{0.01}(pyca)_3(H_2O)_2] \cdot nH_2O$ complex (green line) and $[Y_{0.99}Tb_{0.01}(pyca)_3(H_2O)_2] \cdot nH_2O$ in the inverse opal template voids (black line). Dashed lines represent the linear fitting of the corresponding curves by Eqs. (4, 5) with (a) $D = 2$, $\gamma_A = 20.3 \text{ s}^{-1/3}$ and (b) $D = 3$, $\gamma_A = 35.6 \text{ s}^{-1/2}$. (Adapted from [I].)

As shown above, two additional stages of impurity quenching kinetics may be observed with the increase in donor concentration because of energy migration over donors to acceptors (Eqs. (7-13)). Let us now consider in detail the kinetics of migration accelerated quenching for the powder of the $[\text{Tb}(\text{pyca})_3(\text{H}_2\text{O})_2] \cdot n\text{H}_2\text{O}$ complex. The late stage of it is linearized if the kinetics is represented as $\ln(N(t))$ vs. $t^{1/2}$, but the decay decrement is higher than in the case of the Förster static stage observed for the powder of the $[\text{Y}_{0.99}\text{Tb}_{0.01}(\text{pyca})_3(\text{H}_2\text{O})_2] \cdot n\text{H}_2\text{O}$ complex. This is a signature of the fluctuation stage (Eq. (11)), the decrement of which was determined to be $\gamma_A + \gamma_D = 100.5 \text{ s}^{-1/2}$ (Fig. 6). From this $\gamma_D = 66.5$, and $\alpha = \gamma_A/\gamma_D \approx 0.51$. Note, however, that the best fitting was achieved at $\alpha = 0.52$. Considering Eq. (7), one may see that for a given material, for which C_{DD} and C_{DA} are constant (and for the hopping migration-accelerated quenching $C_{DD} \gg C_{DA}$), α stands for the ratio between the concentration of acceptors other than donors and the concentration of donors. The greater is the ratio, the greater is α . The fluctuation stage begins at $t_f = 1.5 \text{ ms}$. Since $t_s = 0.94 \text{ ms}$, which is very close to t_f , the quasi-stationary migration-accelerated stage could not be observed (Fig. 7).

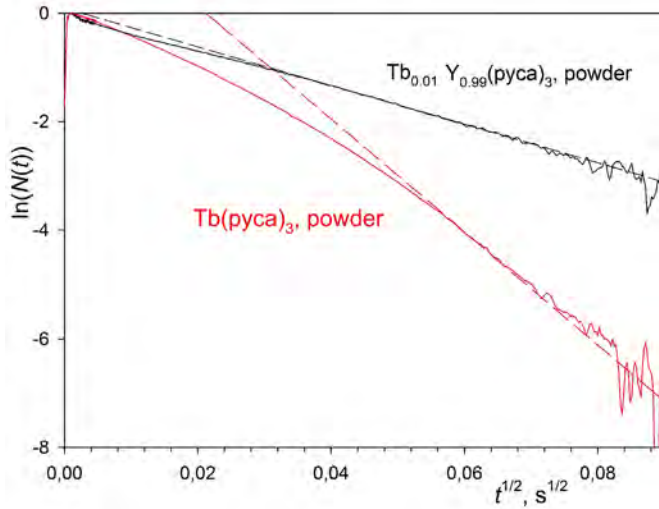


Fig. 6. Energy transfer kinetics of powders of $[\text{Y}_{0.99}\text{Tb}_{0.01}(\text{pyca})_3(\text{H}_2\text{O})_2] \cdot n\text{H}_2\text{O}$ (black curve) and $[\text{Tb}(\text{pyca})_3(\text{H}_2\text{O})_2] \cdot n\text{H}_2\text{O}$ (red curve). The black dashed curve is the fitting by Eqs. (4, 6), the red dashed line is the linear fit by Eq. (11), $\gamma_A + \gamma_D = 100.5 \text{ s}^{-1/2}$. (Adapted from [II].)

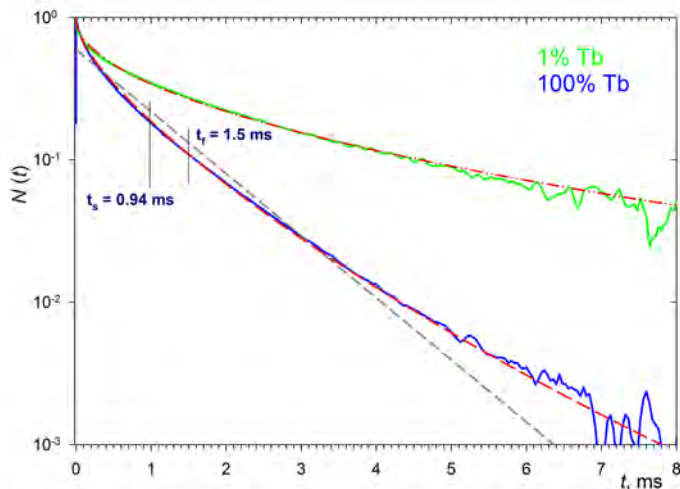


Fig. 7. Energy transfer kinetics of $[\text{Y}_{0.99}\text{Tb}_{0.01}(\text{pyca})_3(\text{H}_2\text{O})_2] \cdot n\text{H}_2\text{O}$ (solid green line) and $[\text{Tb}(\text{pyca})_3(\text{H}_2\text{O})_2] \cdot n\text{H}_2\text{O}$ (solid blue line) complexes as powders. The double dotted – dashed line is the fitting of the static quenching kinetics with the aforementioned parameters. The dashed gray line is the fitting by Eq. (8) with the rate of 1003 s^{-1} . The dashed red line is the complete fitting for the kinetics of migration-accelerated quenching with the aforementioned parameters. (Reproduced with permission from [II].)

5.2. Impurity quenching kinetics of Nd^{3+} doped nanoparticles

As it was shown above, rare-earth doped nanoparticles are of great practical importance for emerging biomedical applications, including fluorescence imaging. Although nanoparticles exhibiting anti-Stokes fluorescence are mainly considered nowadays [3, 6, 7-9, 15, 18, 21-23, 26-35], their emission is in many cases outside the transparency window of the biological tissues (700–1350 nm [11, 13]) and is thus not suitable for deep tumor imaging. To overcome this problem, one may employ near-infrared transitions of rare earths, such as, for example, ${}^4\text{F}_{3/2} - {}^4\text{I}_{9/2}$ transition of Nd^{3+} ion. This strategy, however, has its limitations, since near-infrared fluorescence associated with lower energy optical transitions is more easily quenched by $-\text{OH}$ acceptors than fluorescence in the visible range associated with the higher energy transitions (note that this may be an issue also for the nanoparticles exhibiting anti-Stokes NIR fluorescence, as low-energy transitions transitions are involved). Therefore, studying of the fluorescence quenching mechanisms is of great importance for possible applications. These mechanisms are closely related to many factors, including structural and morphological defects, which may be observed by energy transfer probing. In the course of the current study the energy transfer probe was applied to $\text{Nd}^{3+}:\text{YPO}_4$ and $\text{Nd}^{3+}:\text{KYF}_4$ nanoparticles.

5.2.1. Energy transfer probing of Nd³⁺:YPO₄ nanoparticles

Since fluorescence properties (including fluorescence quenching) are strongly interconnected with structure and morphology of materials, it is necessary to consider these characteristics first. As XRD data reveals (Fig. 8a), both as-prepared and annealed samples of Nd³⁺:YPO₄ nanoparticles consist of the xenotime-type tetragonal phase (Fig. 8b), without a detectable amount of secondary phases. Microwave-hydrothermal treatment for 2 hours allowed us to obtain highly crystalline samples. The degree of crystallinity may be further improved by sample annealing. A typical XRD pattern is similar to the JCPDS reference, which allowed us to use the structural parameters given in the database without further refining.

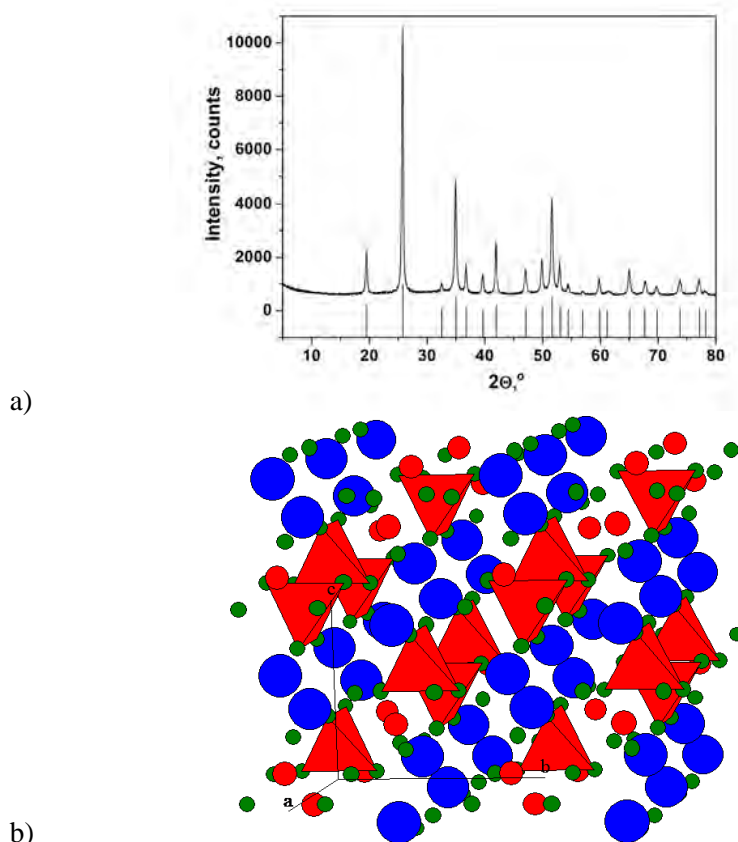


Fig. 8. a) X-ray diffraction pattern of the synthesized yttrium orthophosphate as-prepared nanoparticles and the reference to card #11-254 (tetragonal xenotime-type YPO₄) from JCPDS PDF2 database (adapted from [III]). b) The model of xenotime crystal structure: large blue spheres – yttrium atoms, medium red spheres – phosphorus atoms, small green spheres – oxygen atoms. (Reproduced with permission from [IV]. The structural data are taken from [61, 62].)

Transmission electron microscopy demonstrated that the as-prepared nanoparticles are of about 50 nm in size, their size distribution is rather wide and close to lognormal, which shows that the nanoparticles are aggregated (Fig. 9a,b). However, they could be dispersed to some extent by using ultrasound treatment with surfactants. One hour annealing at 900°C led to much stronger aggregation and substantial growth of the particles, so that they became virtually inseparable (Fig. 9c). Note that particle aggregation and large size allow one to use continuous Förster model valid for bulk crystals [42] while describing the fluorescence quenching kinetics of the nanoparticles.

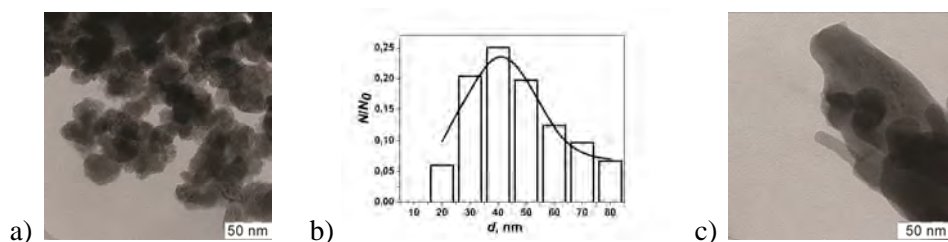
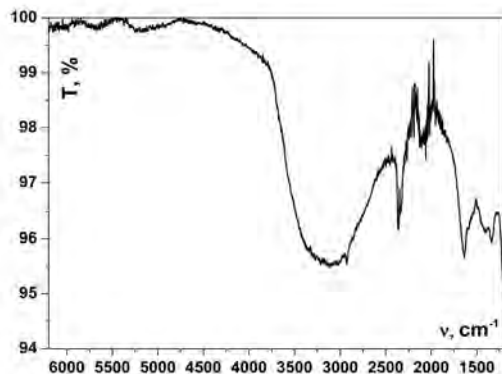
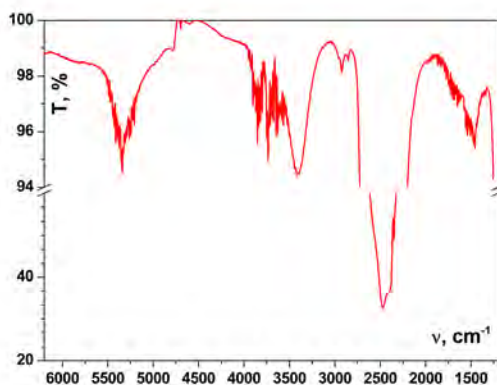


Fig. 9. A TEM image (a) and size distribution (b) of as-prepared phosphate nanoparticles; a TEM image of the same nanoparticles after annealing at 900°C (c). (Adapted from [III, IV].)

Since the samples were synthesized in different media, namely, H₂O and D₂O, one expects respective changes in the vibrational frequencies. The FTIR spectrum of the sample synthesized in water shows an intensive broad band line near 3300 cm⁻¹, associated with –OH vibrations (Fig. 10a). In contrast, the spectrum corresponding to the D₂O colloid demonstrates an intensive band around 2500 cm⁻¹ related to –OD vibrations, while the intensity of the band related to –OH vibrations is lower (Fig. 10b).



a)



b)

Fig. 10. Fragments of FTIR spectra with –OH and –OD vibrations of the powder of phosphate as-prepared nanoparticles synthesized in aqueous media (a) and the colloid of the phosphate nanoparticles in D₂O (b). (Adapted from [III].)

The DTA/DTG curves obtained for the phosphate nanoparticles (Fig. 11) show four minima that were ascribed to the removal of water molecules and –OH groups (the results of mass-spectroscopy of effluent gases were considered). The first peak (maximum rate at ~80°C) was attributed to the removal of H₂O molecules sorbed on the outer nanoparticle surface, bound to the surface by van der Waals forces. The second one (~155°C) was attributed to the removal of –OH groups, which occupy anion sites in the unsaturated coordination spheres of rare-earth ions on the nanoparticle outer surface. Note that since the nanoparticles were re-dried at elevated temperatures (200°C) for considerably long time (2 hours) before the optical measurements, the surface-bound water molecules and –OH groups were mostly removed, so they could not serve as

energy acceptors. As temperature increases further up to 400°C, two additional minima appear, which were associated with the main part of the weight loss. These peaks were ascribed to the removal of the aqueous mother solution from the initially closed mesopores, which supposedly open in this temperature range (~220°C), and the subsequent removal of –OH groups bound to the surface of the opened mesopores (~320°C). Since the pores are situated at different distances from the outer surface of the nanoparticles, and therefore they open at slightly different temperatures, the temperature range corresponding to the process is so wide. The steps of the TG curve are hard to see. This is because, first, there is a continuum of the distances, and second, the water removal is followed by the removal of –OH groups for all the mesopores.

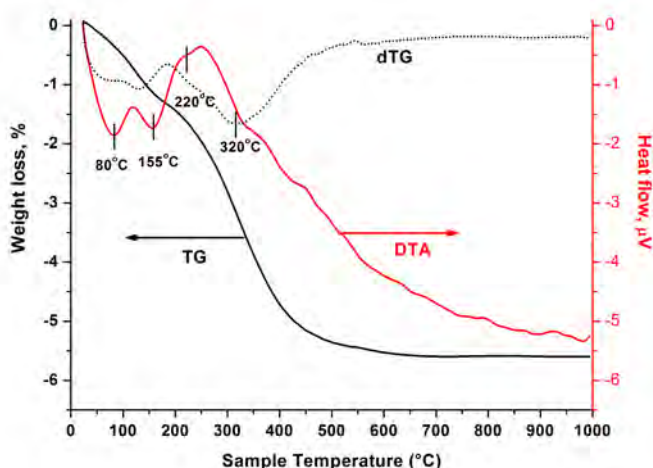


Fig. 11. TG/DTG-DTA curves for the YPO₄ nanoparticles. (Reproduced with permission from [IV].)

The fluorescence excitation spectra of the powders of phosphate nanoparticles synthesized in water were detected at room temperature while tuning the excitation over the ⁴I_{9/2} - ⁴G_{5/2} transition and monitoring the fluorescence at 871.5 nm detection wavelength of the ⁴F_{3/2} - ⁴I_{9/2} transition of Nd³⁺ (Fig. 12a). The fluorescence emission spectra were measured for the same powders at room temperature and at 10 K after excitation of the ⁴G_{5/2} level of Nd³⁺, followed by fast multiphonon relaxation to the ⁴F_{3/2} metastable level (Fig. 12b). The most intensive fluorescence maximum in the biological tissue transparency window corresponds to the 871.5 nm and is due to the ⁴F_{3/2} (2) - ⁴I_{9/2} (1) transition of the Nd³⁺ ion. Annealing of the sample led to the narrowing of the lines due to weaker inhomogeneous broadening, as better crystallinity and less defect structure may be obtained as a result of the thermal treatment.

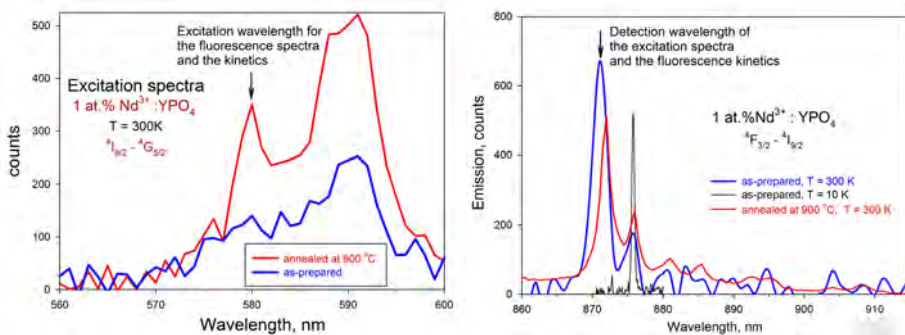


Fig. 12. a) Luminescence excitation spectra with spectral resolution 1.0 nm. Blue line – as-prepared NPs measured at $T = 300$ K, red line – annealed at 900°C ; b) Emission spectra of the 1 at.% $\text{Nd}^{3+}:\text{YPO}_4$ measured with spectral resolution of 0.5 nm: blue line – as-prepared NPs; red line – annealed at 900°C ; black line – the fluorescence spectrum of as-prepared NPs measured at $T = 10$ K (spectral resolution 0.1 nm). Arrows indicate the wavelengths of luminescence excitation (a) and the wavelength of monitoring of the excitation spectra and detection of luminescence kinetics (b). (Reproduced with permission of the PCCP Owner Societies from [III] – <http://pubs.rsc.org/en/Content/ArticleLanding/2014/CP/C4CP03774J>.)

The fluorescence kinetics was detected at room temperature for the powder of the phosphate nanoparticles synthesized in water ($\lambda_{\text{ex}} = 580$ nm, $\lambda_{\text{det}} = 871.5$ nm), for both as-prepared and annealed at 900°C for 1 hour samples. Note that the fluorescence kinetics curves obtained for colloids were identical to those for the powders. As mentioned above, the fluorescence radiative lifetime is normally determined directly from the fluorescence kinetics obtained for the sample with vanishingly small dopant concentrations (to prevent self-quenching and energy migration over donors to acceptors of all types) as the slope of the linearized late stage of the kinetics curve represented as $\ln(I_{\text{meas}})$ vs. t . However, the fluorescence kinetics of the ${}^4\text{F}_{3/2}$ level of the Nd^{3+} ion in the YPO_4 in nanoparticles with 0.1% of the dopant is strongly nonexponential up to late stages (Fig. 13), so the direct determination of the fluorescence radiative lifetime is impossible. However, since the nanoparticles are aggregated, and the structure of the as-prepared nanoparticles does not differ from that of the annealed nanoparticles, one may assume that the radiative lifetime is close for the annealed nanoparticles and for the as-prepared ones. Therefore, the radiative lifetime was determined from the slope of the linearized region of the fluorescence kinetics of the annealed sample to be $\tau_R = 316$ μs (Fig. 14).

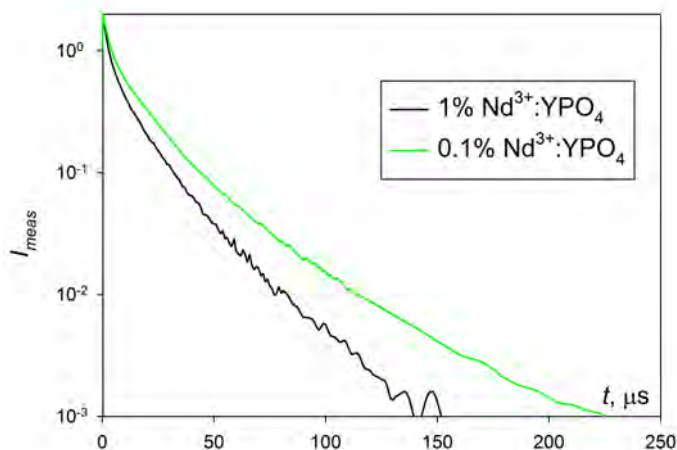


Fig. 13. Fluorescence kinetics of the $\text{Nd}^{3+}:\text{YPO}_4$ as-prepared nanoparticles, dopant concentration 0.1 at.% (green line) and 1 at.% (black line). (Reproduced with permission of the PCCP Owner Societies from [III] – <http://pubs.rsc.org/en/Content/ArticleLanding/2014/CP/C4CP03774J>.)

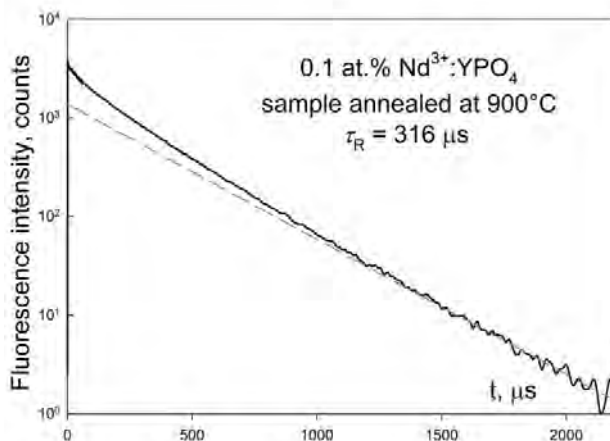


Fig. 14. Fluorescence kinetics of the 0.1 at.% $\text{Nd}^{3+}:\text{YPO}_4$ nanoparticles annealed at 900°C for 1 hour with the indicated fluorescence radiative lifetime. (Reproduced with permission of the PCCP Owner Societies from [III] – <http://pubs.rsc.org/en/Content/ArticleLanding/2014/CP/C4CP03774J>.)

Let us now consider the processes which may lead to the fluorescence quenching in the given system, making the kinetics curve nonexponential. As the scheme (Fig. 15) suggests, for systems containing Nd^{3+} ions in low concentrations and $-\text{OH}$ groups, which are inevitably present in materials synthesized in water, different processes are possible: first, quenching by $-\text{OH}$

acceptors, and second, self-quenching (quenching by Nd^{3+} ions). As the concentration of Nd^{3+} ions increases, energy migration over donors (Nd^{3+}) to acceptors of both types may arise, which accelerates quenching, as shown above.

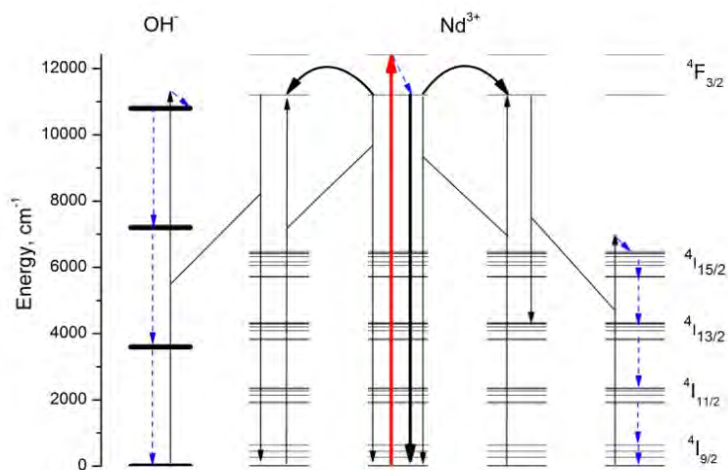


Fig. 15. The scheme of relaxation of the ${}^4\text{F}_{3/2}$ metastable level of the Nd^{3+} ion in the doped crystalline nanoparticles. Red arrow – laser excitation, thick black arrow – near-IR luminescence in the biological tissue transparency window, arc arrows – energy migration over Nd^{3+} ions to unexcited Nd^{3+} ions and to $-\text{OH}$ acceptors, thin black arrows – cross-relaxational transitions which govern nonradiative energy transfer, dashed arrows – multiphonon relaxation. Quenching channels: left – quenching caused by $-\text{OH}$ vibrations; right – self-quenching by unexcited Nd^{3+} ion. (Reproduced with permission of the PCCP Owner Societies from [III] – <http://pubs.rsc.org/en/Content/ArticleLanding/2014/CP/C4CP03774J>.)

Using Eq. (14) and dividing the fluorescence kinetics by the exponential term, one can obtain the impurity quenching kinetics $N(t)$. As shown above, the first stage of static impurity quenching kinetics is the ordered exponential stage (Eqs. 1, 2). This stage, which is related to quenching mostly by acceptors positioned in the nearest coordination spheres of a donor ion, is clearly seen for both 0.1 at.% $\text{Nd}^{3+}:\text{YPO}_4$ and 1 at.% $\text{Nd}^{3+}:\text{YPO}_4$. In the representation $\ln I_{meas}(t)$ vs. t the part of the kinetics corresponding to it was linearized, and its slope is equal to the quenching rate $W_0 = 0.18 \mu\text{s}^{-1}$ in both cases (Fig. 16). Note that the rate does not change as the donor concentration increases, which suggests that self-quenching does not contribute significantly to quenching on this stage. Thus the primary acceptors are $-\text{OH}$ groups, the presence of which in the material structure is confirmed by the result of FTIR analysis. We assume that

these –OH acceptors represent a result of the presence of protonated phosphate groups in the nanoparticle structure, which are positioned close to the donor ions. The reason for this may be that HPO_4^{2-} ions were initially the prevailing form in the reaction mixture, since the precipitation is carried out in the aqueous solution of K_2HPO_4 without pH adjustment, and some of the protonated groups could remain until the end of crystallization, forming the defects.

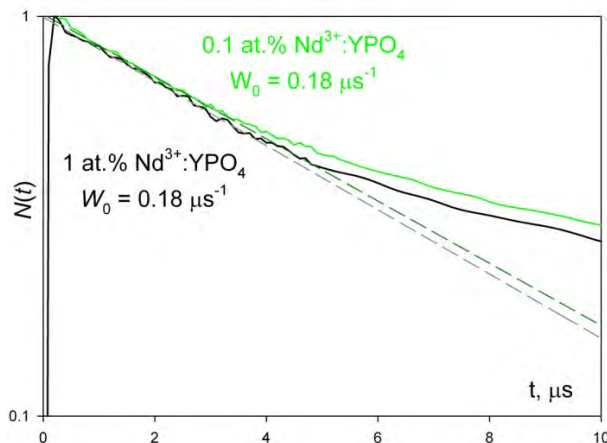


Fig. 16. The ordered stage of the impurity quenching kinetics for the 0.1 at. % $\text{Nd}^{3+}:\text{YPO}_4$ as-prepared sample (green line) and the 1 at.% $\text{Nd}^{3+}:\text{YPO}_4$ as-prepared sample (black line). The dashed curve is the fitting by an exponential decay. (Reproduced with permission of the PCCP Owner Societies from [III] – <http://pubs.rsc.org/en/Content/ArticleLanding/2014/CP/C4CP03774J>.)

In the case of the low Nd^{3+} concentration the initial ordered stage is followed by the transitional region, after which the second stage of static quenching starts, namely, the Förster disordered static quenching (Eq. (4)). This stage is related to quenching by acceptors which are uniformly and equiprobably distributed in the volume of the material and therefore are generally positioned outside the first coordination spheres of the donor ion. Since the donor concentration of 0.1 at.% was found to be too low to detect self-quenching [50], we may limit our consideration to the case of quenching by –OH acceptors. The stages were clearly visible when the kinetics curve was represented as $-\lg(-\ln(N(t)))$ vs. $\lg t$ (Fig. 17). The initial ordered stage is linearized in such representation with the slope of 1. The Förster disordered static stage is also linearized, and the slope, according to Eq. (4), is D/s . In the case under consideration $D/s = 1/2$. A Nd^{3+} –OH interaction is dipole-dipole, and thus $s = 6$. From this $D = 3$, so the acceptor space is three dimensional, as in the case of the powder of Tb^{3+} -containing chelate complexes with 2-pyrazinecarboxylic acid. This means that the –OH acceptors are distributed in the volume of the material. We assume that

they could be found in the form of molecular water in the mesopores and –OH groups on the mesopore surface. The formation of mesopores, filled with mother solution (in the case under consideration – aqueous), is described elsewhere [63, 64]. The mesopores containing acceptors are uniformly and equiprobably distributed, and thus averaging over all sites yields the well-known Förster kinetics.

Plotting the kinetics curve for the 0.1 at.% Nd³⁺:YPO₄ nanoparticles as $\ln N(t)$ vs. $t^{D/s} = t^{1/2}$ (Fig. 18), one may find the macroparameter of donor-acceptor interactions γ_A as a slope of the linearized part of the curve (Eq. (4)) to be $\gamma_A = 0.484 \mu\text{s}^{-1/2}$. Since the donor-acceptor interactions are dipole-dipole, one may use Eq. (6) to estimate the absolute acceptor concentration in the material. Considering that the value of C_{DA} (microparameter of donor-acceptor interactions) for phosphate nanoparticles is close to that obtained for phosphate glasses, $C_{DA}(\text{Nd} - \text{OH}) = 0.6 \text{ nm}^6/\text{ms}$ [44, 65], one may estimate $n_A(\text{OH}) = 1.66 \text{ nm}^{-3}$. From the structural parameters $n_A(\text{Nd}^{3+}) = 0.014 \text{ nm}^{-3}$ for 0.1 at.% of Nd³⁺ and $n_A(\text{Nd}^{3+}) = 0.14 \text{ nm}^{-3}$ for 1 at.% of Nd³⁺, which is significantly less than $n_A(\text{OH})$. Correspondingly, the minimal distance between a Nd³⁺ ion and an –OH acceptor ($R_{\min}(\text{Nd} - \text{OH}) \approx 0.23 \text{ nm}$ [66], which is significantly shorter than that between two neighboring Nd³⁺ ions ($R_{\min}(\text{Nd} - \text{Nd}) = 0.3758 \text{ nm}$ [67]), and thus has a significantly larger contribution to the energy transfer rate in the donor – acceptor pair, determined by:

$$W_{DA} = C_{DA}/R_{\min}^6 \quad (15)$$

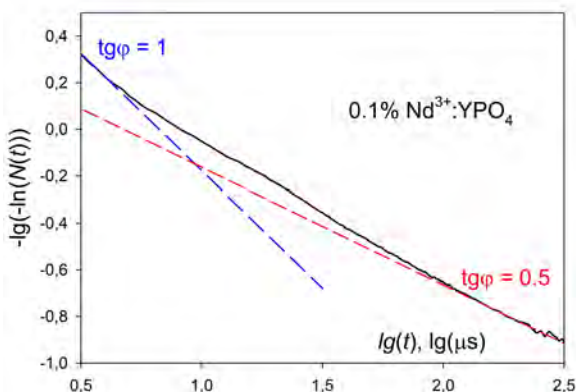


Fig. 17. The impurity quenching kinetics of the 0.1 at.% Nd³⁺:YPO₄ as-prepared sample represented as $-\lg(-\ln(N(t)))$ vs. $\lg t$. (Reproduced with permission of the PCCP Owner Societies from [III] – <http://pubs.rsc.org/en/Content/ArticleLanding/2014/CP/C4CP03774J>.)

Therefore, the contribution of self-quenching is negligibly small in comparison with that of quenching by $-OH$ acceptors for both the lower and higher dopant concentrations.

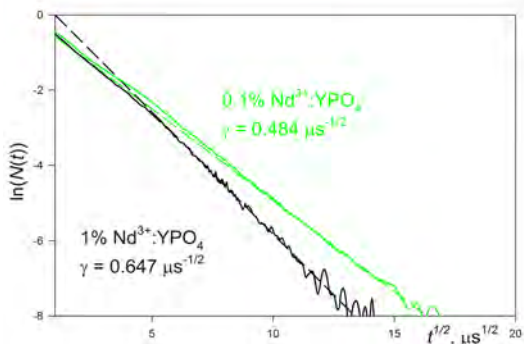


Fig. 18. The disordered stage of the impurity quenching kinetics for the 0.1 at.% $Nd^{3+}:YPO_4$ as-prepared sample (green line) and the 1 at.% $Nd^{3+}:YPO_4$ as-prepared sample (black line). The green dashed curve is the fitting by Eqs. (4, 6), the black dashed curve is the fitting curve by Eq. (11). (Reproduced with permission of the PCCP Owner Societies from [III] – <http://pubs.rsc.org/en/Content/ArticleLanding/2014/CP/C4CP03774J>.)

The case of the higher donor concentration (1 at.% of $Nd^{3+}:YPO_4$) is more complicated than that of the vanishingly small donor concentration, because migration over donors to acceptors accelerates quenching, which is not static anymore. As it may be seen (Fig. 18), the late stage of the kinetics curve is also linearized in the given representation, but the decay decrement is greater than in the case of 0.1 at.% of $Nd^{3+}:YPO_4$, so this part of the kinetics curve could be attributed to the fluctuation stage of migration accelerated quenching. The slope of the linearized part of the kinetics curve in this case is equal to $\gamma_A + \gamma_D$ [49-51], so $\gamma_A + \gamma_D = 0.647 \mu s^{-1/2}$, and thus $\gamma_D = 0.163 \mu s^{-1/2}$. The parameter α may be therefore found according to Eq. (13): $\alpha \approx 2.95$, so $\alpha > 1$. Furthermore, one may find the C_{DD} microparameter of donor-donor interactions using Eq. (12) to be $C_{DD} = 24.6 \text{ nm}^6/\text{ms}$, so it is almost 2 orders of magnitude greater than $C_{DA}(Nd - OH) = 0.6 \text{ nm}^6/\text{ms}$. These two facts confirm that we deal with the fluctuation stage of hopping migration accelerated quenching. Another question is if it is the only stage of migration accelerated quenching one could observe. This may be tested by determination of the boundary time values t_s and t_f (Eq. (10)). In the case under consideration $t_s = 150 \mu s > t_f = 3 \mu s$, so no time range could be associated with the quasi-stationary migration-accelerated stage, and the fluctuation quenching is the only realizing stage of migration accelerated quenching.

Plotting the kinetics curve related to 1 at.% of $Nd^{3+}:YPO_4$ nanoparticles as $-\lg(-\ln(N(t)))$ vs. $\lg t$ (Fig. 19), one might see both stages considered above for this sample, namely, the ordered static one (slope 1) and the fluctuation

migration accelerated one. The slope of the fluctuation stage is 1/2. This additionally confirms that donor and acceptor spaces are 3-dimensional, so –OH acceptors are likely distributed in the mesopores of the nanoparticles.

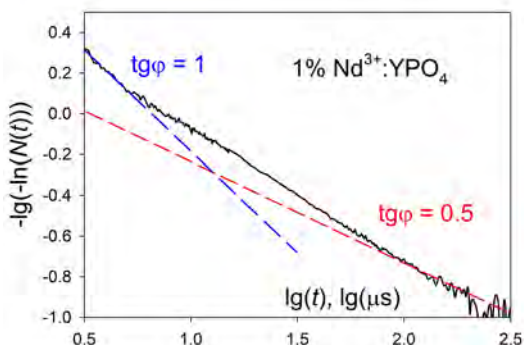


Fig. 19. The impurity quenching kinetics of the 1 at.% $\text{Nd}^{3+}:\text{YPO}_4$ as-prepared sample represented as $-\lg[-\ln(N(t))]$ vs. $\lg t$. (Reproduced with permission of the PCCP Owner Societies from [III] – <http://pubs.rsc.org/en/Content/ArticleLanding/2014/CP/C4CP03774J>.)

Thus energy transfer probing suggests that there are two types of –OH acceptors in the system: first, the ones associated with protonated phosphate groups and contributing to the initial ordered stage of static quenching; and second, the ones positioned in mesopores and contributing to the late stage of quenching (Fig. 20). These results were tested by other techniques.

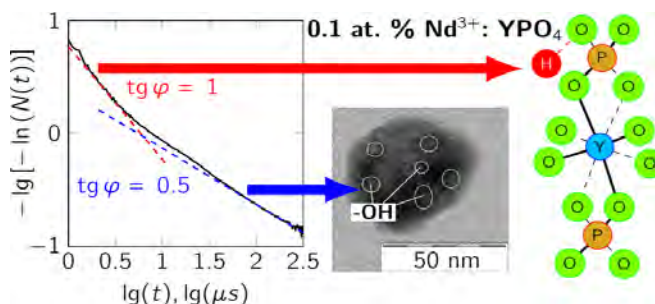


Fig. 20. The initial ordered stage corresponds to quenching by both types of acceptors, while the disordered stage – only to quenching by acceptors positioned in mesopores. (Reproduced with permission of the PCCP Owner Societies from [III] – <http://pubs.rsc.org/en/Content/ArticleLanding/2014/CP/C4CP03774J>. The structural data are taken from [61, 62].)

First, let us consider the fluorescence kinetics (Fig. 21a) and quenching kinetics (Fig. 21b) obtained for the deuterated colloids of the nanoparticles prepared in the D₂O (the consideration is limited to the vanishingly small dopant concentration to exclude energy migration). As FTIR results suggest, –OD vibrations are low-energy ones, and thus quenching by them is much less probable than quenching by high-energy –OH vibrations. The data of fluorescence kinetics spectroscopy confirm that the level of quenching for the deuterated sample is much lower than that for the nanoparticles prepared in the aqueous medium, while no difference was detected for the powders and colloids of the latter. Note that no ordered stage of static quenching was detected for the deuterated sample, which confirms the hypothesis that this stage is related to quenching arising as a result of the presence of protonated –OH groups in the material structure, since no significant amount of the –OH groups could be associated with the protonated phosphate groups in the deuterated sample. Moreover, plotting the kinetics curves as $\ln N(t)$ vs. $t^{1/2}$ (Fig. 22) and calculating the values of macroparameters of donor-acceptor interaction as described above, one can see that the one obtained for the deuterated sample ($\gamma_A(\text{OD}) = 0.201 \mu\text{s}^{-1/2}$) is more than two times as less as the one found for the water-based sample ($\gamma_A = 0.484 \mu\text{s}^{-1/2}$).

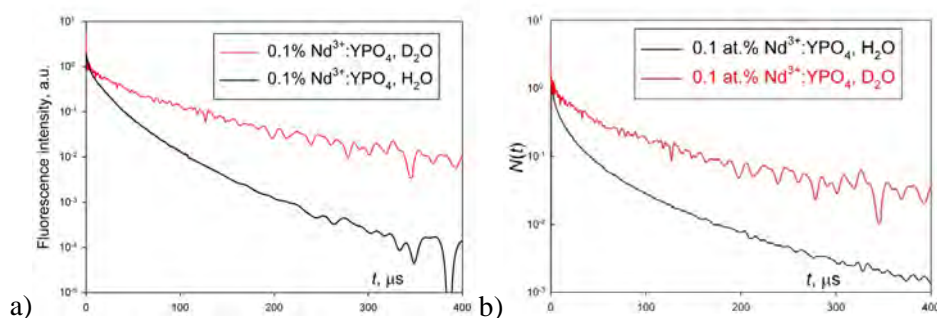


Fig. 21. Fluorescence kinetics (a) and impurity quenching kinetics (b) of the 0.1 at.% Nd³⁺:YPO₄ nanoparticles synthesized in D₂O (colloid, red line) and H₂O (powder, as-prepared, black line). (Reproduced with permission of the PCCP Owner Societies from [III] – <http://pubs.rsc.org/en/Content/ArticleLanding/2014/CP/C4CP03774J>.)

Second, the conclusion made by using energy transfer probing is also confirmed by the results of the TG and DTA/DTG analysis. The surface-bound water molecules and –OH groups were likely removed in the course of the thermal treatment, preceding fluorescent measurement. The process of mesopore opening might also start during the particle drying, but the major part of mesopores likely remained closed and thus filled with mother solution during the optical measurements. Therefore, the –OH acceptors associated with the mesopores, could participate in the quenching process.

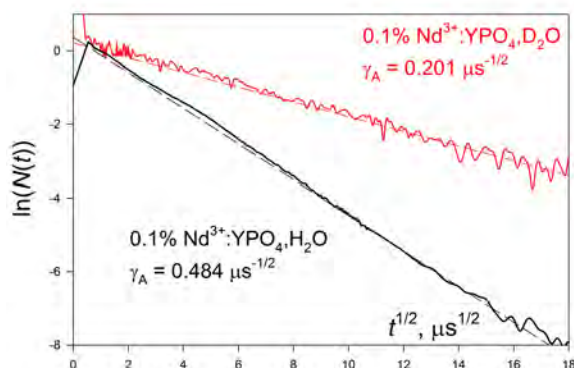


Fig. 22. Impurity quenching kinetics of the as-prepared 0.1 at.% Nd^{3+} : YPO_4 nanoparticles in D_2O (colloid, red line) and H_2O (black line) in the scales of $\ln(N(t))$ vs. $t^{1/2}$. The dashed curves represent the fitting by Eqs. (4, 6). (Reproduced with permission of the PCCP Owner Societies from [III] – <http://pubs.rsc.org/en/Content/ArticleLanding/2014/CP/C4CP03774J>.)

To sum up, it was shown that the main source of fluorescence quenching in Nd^{3+} : YPO_4 nanoparticles synthesized in aqueous medium is the presence of the $-\text{OH}$ acceptors. This makes the nanoparticles remarkably different from Nd^{3+} doped bulk crystals, where only Nd - Nd self-quenching accelerated by hopping energy migration was found. In the latter case $\alpha \ll 1$, and the migration accelerated quenching kinetics is exponential over a long time range, so the fluctuation stage cannot be detected.

By means of energy transfer probing it was shown that there are two types, or locations, of energy acceptors in the structure of the nanoparticles: first, the ones associated with the protonated groups, and thus located close to the donor Nd^{3+} ions, and second, the ones located in the mesopores (at longer distances from the donor ions). The results obtained for the deuterated colloids of the phosphate nanoparticles synthesized in deuterium oxide and the TG-DTA/DTG data, obtained for the powders of the nanoparticles synthesized in H_2O , indirectly prove this conclusion. Note that since the $-\text{OH}$ acceptors are distributed in the volume of the material, one could not eliminate quenching entirely by coating the surface of the nanoparticle with a protective layer.

5.2.2. Energy transfer probing of Nd^{3+} : KYF_4 nanoparticles

Complex fluorides are now considered as very perspective matrices for strongly fluorescent rare-earth doped nanoparticles. One of the factors which play an important role here is the relatively long distances between the dopant sites, which result in low level of self-quenching in the material. In this section

$\text{Nd}^{3+}:\text{KYF}_4$ nanoparticles will be compared with $\text{Nd}^{3+}:\text{YPO}_4$ nanoparticles using results of energy transfer probing.

First, let us consider the structure and morphology of the material. A typical XRD pattern (Fig. 23) is similar to the ones reported in [58, 59] as corresponding to the cubic modification of KYF_4 (space group Fm-3m). The lines are only slightly shifted from the references, probably due to the different dopant ion and its concentration. According to the XRD data, the material contains only a negligibly small amount of secondary phases and is well-crystalline (the degree of crystallinity is higher than that for the phosphate nanoparticles), so the number of defects, which energy acceptors can be associated with, is less.

According to TEM data (Fig. 24), the nanoparticles are isotropic and quite uniform, of the mean diameter around 30-40 nm. Note that the mesopores might be seen in TEM images.

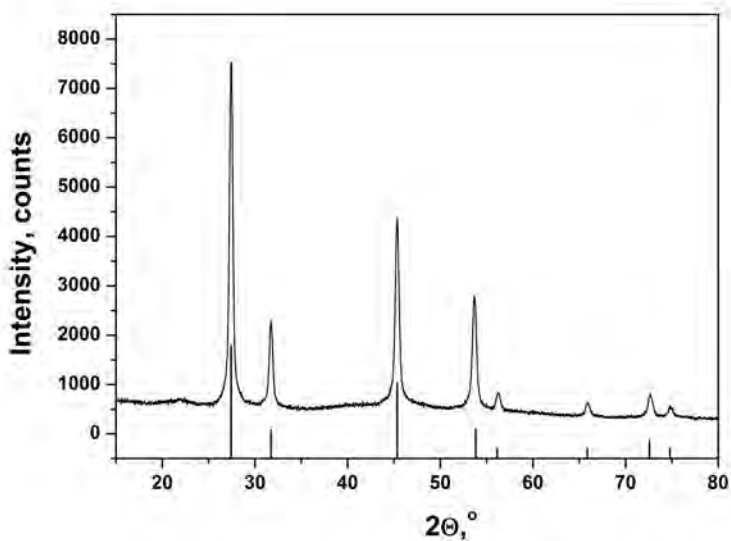


Fig. 23. X-ray diffraction pattern of as-prepared yttrium fluoride nanoparticles (reproduced with permission from [V]).

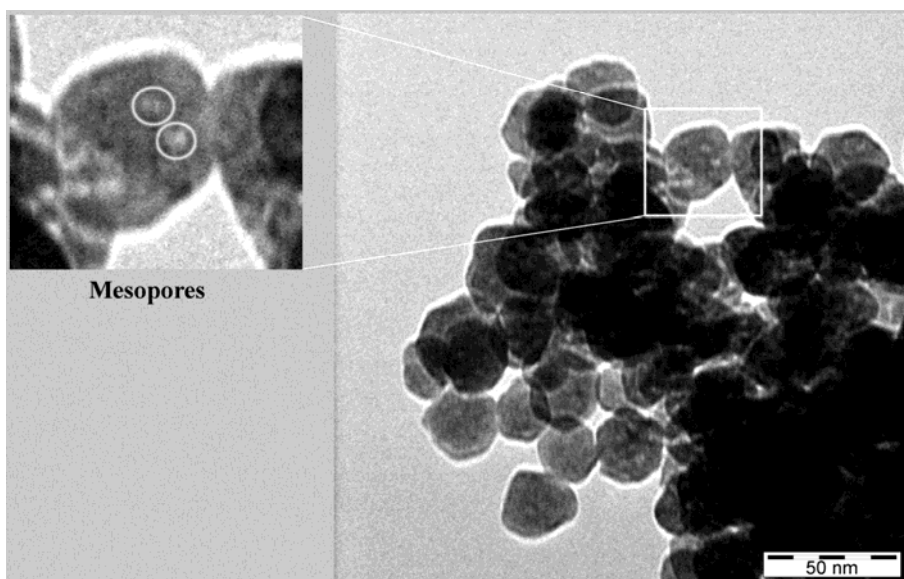


Fig. 24. TEM images of the $\text{Nd}^{3+}:\text{KYF}_4$ nanoparticles; the inset shows a zoomed fragment demonstrating the presence of the mesopores. (Reproduced with permission from [V].)

The major part of the weight loss according to the TG data with mass-spectroscopy of effluent gases is associated with H_2O and $-\text{OH}$. The DTA/DTG curves show two wide minima for the loss of H_2O and $-\text{OH}$ (Fig. 25). The low-temperature one (maximal rate $\sim 107^\circ\text{C}$ according to the DTA data) was attributed to the removal of the physisorbed H_2O molecules, followed by the removal of chemisorbed $-\text{OH}$ groups from the outer surface of the nanoparticles. The higher-temperature one (maximal rate at $\sim 232^\circ\text{C}$) could be ascribed to the opening of the mesopores and the removal of H_2O molecules and $-\text{OH}$ groups from them. Note that one can observe only one well-pronounced minimum associated with the mesopore opening for the fluoride nanoparticles, whereas an additional higher-temperature ($\sim 320^\circ\text{C}$) one may be seen only for the phosphate nanoparticles (Fig. 11), as the KYF_4 nanoparticles are smaller and thus the formation of deep mesopores is unlikely.

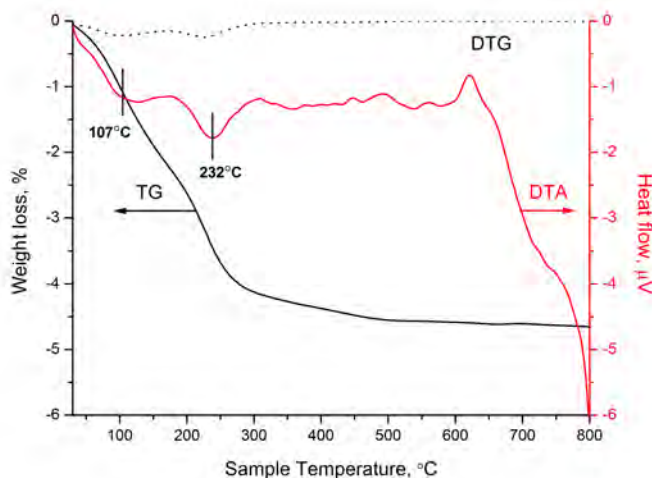


Fig. 25. TG/DTG-DTA curves for the KYF_4 nanoparticles.

To assess dispersibility of the nanoparticles in aqueous medium without application of potentially toxic surfactants, which is an important characteristic of a material intended for biomedical applications, two samples of the fluoride nanoparticles were prepared using the Emuksol-268 poloxamer as a biocompatible surfactant. The sample 1 which was prepared with the poloxamer addition before gel precipitation showed good dispersibility after short duration ultrasound treatment (Fig. 26, gray bars). The hydrodynamic radius of these nanoparticles is ~ 20 nm; and the size distribution is narrow and close to normal. Therefore, taking into account that the hydrodynamic radius is normally larger than the nanoparticle radius estimated from the TEM data, one may conclude that a colloidal solution of individual nanoparticles is formed. On the contrary, the nanoparticles of the sample 2 synthesized with the late addition of Emuksol-268 (after gel precipitation) are strongly agglomerated, and could not be dispersed by moderate ultrasonication. The mean radius of the aggregates according to the DLS data exceeds 200 nm; and the size distribution is close to lognormal (Fig. 26, hatched bars), which suggests that the nanoparticle aggregation is fast.

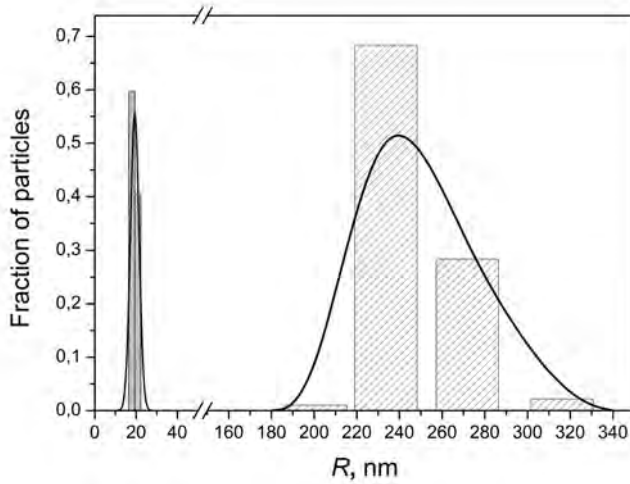


Fig. 26. Fractions of the particles of the corresponding hydrodynamic radii according to the DLS data: the sample 1 (gray bars) is prepared with the addition of the surfactant directly to the mixture of $\text{Y}(\text{NO}_3)_3 \cdot 4\text{H}_2\text{O}$ and $\text{Nd}(\text{NO}_3)_3 \cdot 5\text{H}_2\text{O}$ solutions before gel precipitation; the sample 2 (hatched bars) is prepared with the addition of the surfactant after gel precipitation; the solid lines indicate the corresponding distributions. (Reproduced with permission from [V].)

The fluorescence excitation spectra of the 0.1 at.% $\text{Nd}^{3+}:\text{KYF}_4$ were measured at 10 K and at room temperature (Fig. 27a) at $\lambda_{det} = 865$ nm, corresponding to the ${}^4\text{F}_{3/2} - {}^4\text{I}_{9/2}$ transition of the Nd^{3+} ion. The excitation maximum observed at $\sim 550\text{--}600$ nm was attributed to the ${}^4\text{I}_{9/2} - {}^4\text{G}_{5/2}; {}^2\text{G}_{7/2}$ absorption transition. Site-selective fluorescence spectra (Fig. 27b) were detected at 10 K at the ${}^4\text{F}_{3/2} - {}^4\text{I}_{9/2}$ NIR optical transition after direct excitation into the ${}^4\text{G}_{5/2}$ level and subsequent fast multiphonon relaxation to the ${}^4\text{F}_{3/2}$ level of Nd^{3+} ion by tuning the excitation wavelength of the OPO laser with the step of 1 nm to the long wavelength starting from 576 nm (along the long-wavelength wing of the absorption line). The represented spectra demonstrate that there are two optical sites in the system, and their concentrations may be regarded to be approximately equal, since the intensities of the fluorescence maxima of the sites are close [68]. One of them could be selectively excited at longer λ_{exc} , but is, however, of less importance regarding potential applications, since the fluorescence transition corresponding to it is shifted to NIR and lies farther in the IR spectral range from the sensitivity range of most detectors. The fluorescence kinetics of the ${}^4\text{F}_{3/2}$ level of Nd^{3+} was detected at $\lambda_{det} = 857.5$ nm after excitation at $\lambda_{exc} = 575.5$ nm. Although this excitation wavelength does not provide the selective excitation of this type of optical sites, it is possible to detect its fluorescence kinetics separately at the short-wavelength wing of the fluorescence line corresponding to this site.

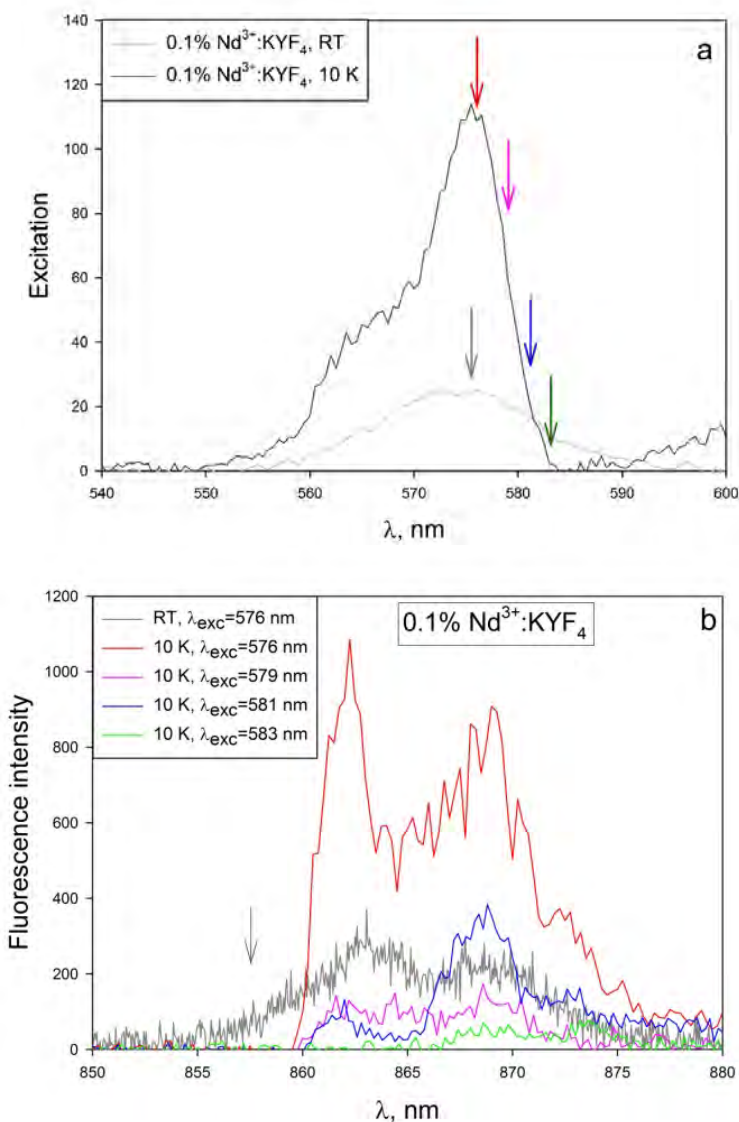


Fig. 27. The fluorescence excitation (a) and emission (b) spectra of the 0.1 at.% $\text{Nd}^{3+}:\text{KYF}_4$ nanoparticles measured at two different temperatures. The fluorescence excitation spectra are detected at 861 nm at the $^4\text{F}_{3/2} - ^4\text{I}_{9/2}$ transition of Nd^{3+} , arrows indicate the excitation wavelengths at which the fluorescence spectra were recorded: gray – 575.5 nm, red – 576 nm, pink – 579 nm, blue – 581 nm, green – 583 nm (adapted from [V]). The fluorescence emission spectra are detected after excitation into the $^4\text{G}_{5/2}$ level of Nd^{3+} at indicated wavelengths; the arrow indicates the detection wavelength of the fluorescence kinetics measurement. (Reproduced with permission from [V].)

The fluorescence kinetics of the 0.1 at.% $\text{Nd}^{3+}:\text{KYF}_4$ nanoparticles synthesized in water is nonexponential up to late stages (Fig. 28, black curve) due to fluorescence quenching, so the direct determination of the fluorescence radiative lifetime is not possible. Note that the average $\text{Nd}^{3+}\text{-Nd}^{3+}$ distance is longer in KYF_4 ($R_{\text{av}} > 2.1$ nm) than in YPO_4 ($R_{\text{av}} \sim 1.9$ nm), where self-quenching was shown to be insignificant. Therefore, it is unlikely that self-quenching plays a significant role for the fluoride Nd^{3+} -doped nanoparticles. Thus fluorescence quenching in the system was assumed to be caused primarily by $-\text{OH}$ energy acceptors. High-temperature treatment of fluoride materials in air may cause their oxidation, and therefore could not be applied to eliminate $-\text{OH}$ acceptors, as in the case of phosphates. Instead, in order to determine τ_R , the fluorescence kinetics of the deuterated sample was measured, from which the radiative lifetime value was found as described above to be $\tau_R = 1862$ μs (Fig. 28, green curve), which is almost 6 times longer than that obtained for the $\text{Nd}^{3+}:\text{YPO}_4$ nanoparticles ($\tau_R = 316$ μs).

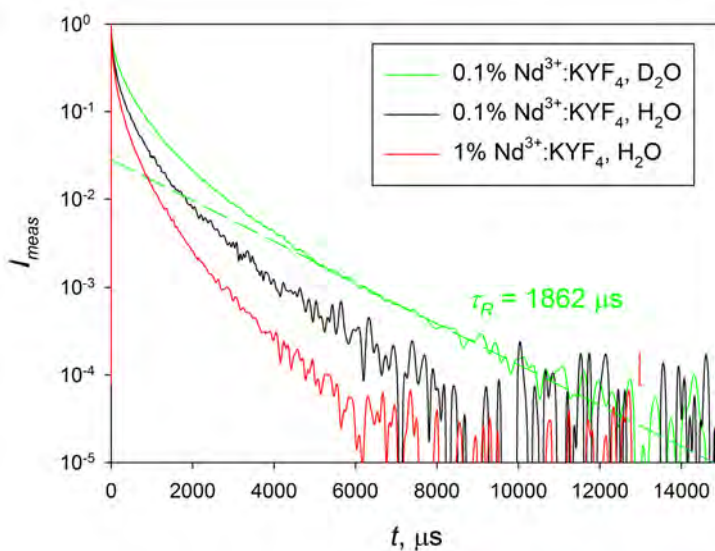


Fig. 28. Fluorescence kinetics of the $\text{Nd}^{3+}:\text{KYF}_4$ nanoparticles: synthesized in D_2O , Nd^{3+} concentration 0.1 at.% (green line); synthesized in H_2O , Nd^{3+} concentration 0.1 at.% (black line) and 1 at.% (red line), $\lambda_{\text{exc}} = 575.5$ nm, $\lambda_{\text{det}} = 857.5$ nm; the dashed line is the fitting by the exponential function. (Reproduced with permission from [V].)

The impurity quenching kinetics of the 0.1 at.% $\text{Nd}^{3+}:\text{KYF}_4$ nanoparticles synthesized in water was obtained as shown previously by division of the fluorescence kinetics by the exponential term (Eq. (14)). Taking into account the fact that the average $\text{Nd}^{3+}\text{-Nd}^{3+}$ distance is longer for the fluoride nanoparticles than that for the phosphate ones and the fluorescence radiative

lifetime is also longer for the fluoride ones, one may conclude that energy migration is negligible for 0.1 at.% $\text{Nd}^{3+}:\text{KYF}_4$ nanoparticles, therefore, only static quenching may be considered in this case. The Förster disordered stage was identified by plotting the kinetics curve as $-\lg(-\ln(N(t)))$ vs. $\lg t$ (Fig. 29, black curve). The slope of the linearized part of the curve in this representation is $1/2$, similar to previously considered case of the phosphate nanoparticles. Similarly, the dimensionality of the acceptor space $D = 3$, so acceptors are distributed in the volume of the material. Considering the results of TEM microscopy (Fig. 24), one could assume that the source of quenching is the same as in the case of $\text{Nd}^{3+}:\text{YPO}_4$ nanoparticles, namely, $-\text{OH}$ acceptors positioned in mesopores formed during the material crystallization. This result is indirectly confirmed by the fact that quenching is significantly reduced in the deuterated sample. Note that in the case under consideration the fluorescence kinetics does not finish with the Förster stage, as the slowing down of the kinetics may be observed after it. This effect might be due to the finite sizes of nanoparticles, since restricted nanoparticle volume means that the number of acceptors surrounding a donor ion, positioned in a thin surface layer, is limited in comparison with the number of acceptors surrounding a donor ion, positioned in the volume of the material [69].

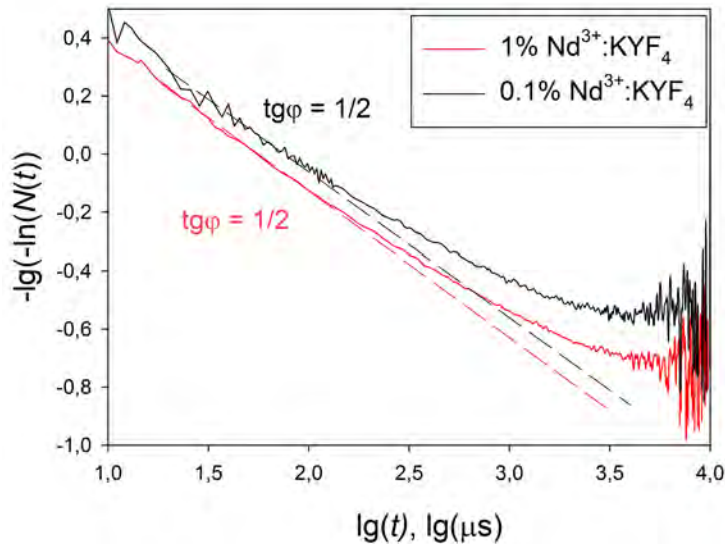


Fig. 29. Impurity quenching kinetics $N(t)$ represented as $-\lg(-\ln(N(t)))$ vs. $\lg t$, 0.1 at.% of Nd^{3+} – black line and 1 at.% of Nd^{3+} – red line, the dashed lines correspond to the slope of $1/2$. (Adapted from [V].)

Plotting the kinetics curve corresponding to 0.1 at.% $\text{Nd}^{3+}:\text{KYF}_4$ nanoparticles as $\ln N(t)$ vs. $t^{1/2}$ (Fig. 30), one could find the value of the donor-acceptor interaction macroparameter γ_A as described above to be $\gamma_A = 0.113 \mu\text{s}^{-1/2}$. Taking into account the fact that the C_{DA} microparameter is proportional to the spontaneous emission rate $A = 1/\tau_R$ for the excited state of the donor [42, 70], we estimated the C_{DA} value from the ratio of the spontaneous emission rates in the fluoride and phosphate nanoparticles (considering $C_{DA} = 0.6 \text{ nm}^6/\text{ms}$ for the latter) to be $C_{DA} \approx 0.1 \text{ nm}^6/\text{ms}$ for the $\text{Nd}^{3+}:\text{KYF}_4$ nanoparticles. Subsequently, the concentration of $-\text{OH}$ acceptors was estimated to be $n_A = 1.5 \text{ nm}^{-3}$, using Eq. (6). This is approximately two times lower than the concentration of $-\text{OH}$ acceptors in the $\text{Nd}^{3+}:\text{YPO}_4$ nanoparticles ($n_A = 2.7 \text{ nm}^{-3}$).

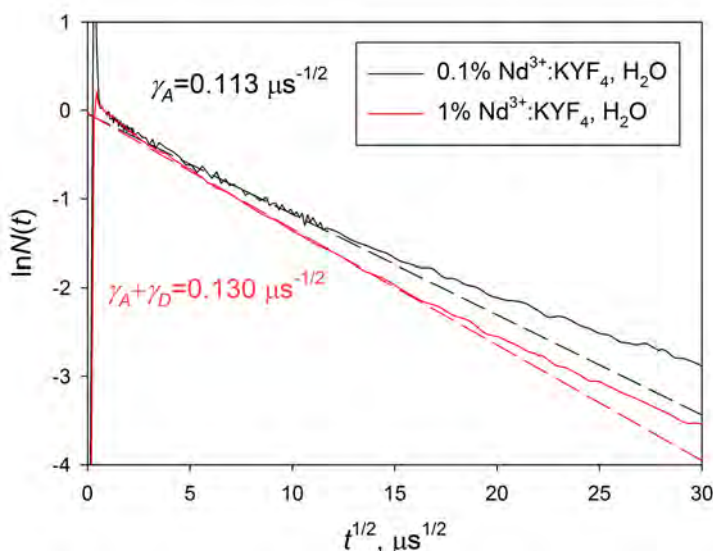


Fig. 30. Impurity quenching kinetics $N(t)$ represented as $\ln(N(t))$ vs. $t^{1/2}$, 0.1 at.% of Nd^{3+} – black line and 1 at.% of Nd^{3+} – red line. The black dashed curve is the fitting by Eqs. (4, 6), the red dashed curve is the fitting curve by Eq. (11). (Reproduced with permission from [V].)

Similar to the case of the phosphate nanoparticles, the increase in the dopant concentration from 0.1 at.% to 1 at.% results in migration acceleration of quenching. The intermediate stage of the kinetics is linearized when the kinetics curve was represented as $-\lg(-\ln(N(t)))$ vs. $\lg t$ with the slope of 1/2 (Fig. 29), which was associated with the fluctuation stage of migration accelerated quenching in three dimensional donor and acceptor spaces. The intermediate part of the curve is also linearized when the kinetics curve is plotted as $\ln(N(t))$ vs. $t^{1/2}$ with the decrement greater than that of the Förster static stage detected

for 0.1 at.% $\text{Nd}^{3+}:\text{KYF}_4$ nanoparticles (Fig. 30), which confirms that the fluctuation stage is observed. As found from its slope, $\gamma_D + \gamma_A = 0.130 \mu\text{s}^{-1/2}$, and thus $\gamma_D = 0.017 \mu\text{s}^{-1/2}$. Considering the concentration of one type of optical sites to be one half from the total Nd^{3+} concentration, $n_i^{(\text{OC})} = 4.91 \cdot 10^{-2} \text{ nm}^{-3}$, one could find $C_{DD} = 2.17 \text{ nm}^6/\text{ms}$ for the fluoride nanoparticles, which is more than one order of magnitude less than $C_{DD} = 24.6 \text{ nm}^6/\text{ms}$ obtained for the phosphate nanoparticles. Note that $C_{DD} \gg C_{DA}$, which confirms that quenching is hopping, whereas $\alpha \approx 6.6 > 1$ signifies that the fluctuation stage is observed. Also, note that as in the case of the phosphate nanoparticles, the Nd^{3+} concentration in the fluoride nanoparticles is significantly less than that of $-\text{OH}$ acceptors.

Thus energy transfer probing of the Nd^{3+} -doped nanoparticles consisting of the cubic modification of KYF_4 revealed that the $-\text{OH}$ quenchers are distributed in the material volume, presumably, in the mesopores, which is indirectly proven by the TEM data. The slowing down of the kinetics at the late stage is consistent with the fact that the fluoride nanoparticles are smaller and more easily dispersible than the phosphate ones, which is confirmed by TEM and DLS results (Fig. 31).

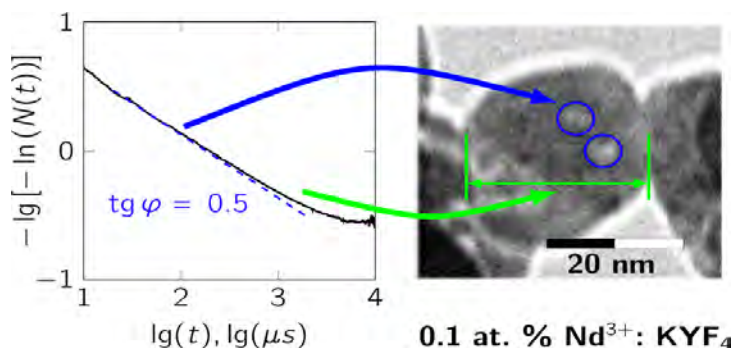


Fig. 31. The disordered stage corresponds to quenching by acceptors in mesopores; the slowing down of the late stage of the kinetics may be explained by the particle restricted geometry.

The values of micro- and macroparameters of quenching and energy migration, obtained for the fluoride nanoparticles, are less than those for the phosphate nanoparticles, which means that both processes are less effective in fluorides (Table 1). Also, the concentration of $-\text{OH}$ acceptors is lower in the fluoride nanoparticles than in the phosphate ones. For both matrices, using D_2O instead of H_2O leads to substantial suppression of fluorescence quenching.

Table 1. Comparison of the radiative lifetimes and quenching parameters for the Nd³⁺:YPO₄ and Nd³⁺:KYF₄ nanoparticles synthesized in different media.

Matrix	$n(\text{Nd}^{3+})$, at. %	Solvent	τ_R , μs	W_{0_2} , μs^{-1}	γ_A , $\mu\text{s}^{-1/2}$	γ_D , $\mu\text{s}^{-1/2}$	c_{DA} , nm^6/ms	c_{DD} , nm^6/ms	$n_D(\text{Nd}^{3+})$, nm^{-3}	$n_A(-\text{OH})$, nm^{-3}
YPO ₄	0.1	H ₂ O	316	0.18	0.484	-	0.6	-	0.014	2.7
YPO ₄	1	H ₂ O	316	0.18	0.484	0.163	0.6	24.6	0.14	2.7
YPO ₄	0.1	D ₂ O	316	-	0.201	-	?	-	0.014	?
KYF ₄	0.1	H ₂ O	1862	-	0.113	-	0.1	-	$4.91 \cdot 10^{-3*}$	1.5
KYF ₄	1	H ₂ O	1862	-	0.113	0.017	0.1	2.17	$4.91 \cdot 10^{-2*}$	1.5
KYF ₄	0.1	D ₂ O	1862	-	0.066	-	?	-	$4.91 \cdot 10^{-3*}$?

- not possible to calculate because the corresponding stage could not be observed

? not possible to calculate because of unidentifiable contributions of -OH and -OD acceptors

* for one type of optical sites

From the practical viewpoint, it is useful to compare fluorescence quantum yield of the phosphate and fluoride nanoparticles with the same dopant and dopant concentration (for example, 0.1 at. % of Nd³⁺). The fluorescence quantum yield η of the ⁴F_{3/2} metastable level of the Nd³⁺ ion may be calculated as [71]:

$$\eta = \frac{1}{\tau_R} \int_0^{\infty} I_{meas}(t) dt \quad (16)$$

Omitting the details, one may note that the fluorescence quantum yield decreases with the increase of γ_A , which is a quantitative parameter for quenching by -OH acceptors distributed in volume of the nanoparticles (Table 2). This confirms that quenching is mainly caused by -OH acceptors distributed in the nanoparticle volume.

Table 2. Comparison of the fluorescence quantum yields and quenching macro-parameters for the 0.1 at.% Nd³⁺:YPO₄ and 0.1 at.% Nd³⁺:KYF₄ nanoparticles synthesized in different media.

Matrix	$n(\text{Nd}^{3+})$, at. %	Solvent	τ_R , μs	γ_A , $\mu\text{s}^{-1/2}$	η , %
YPO ₄	0.1	H ₂ O	316	0.484	4.50
YPO ₄	0.1	D ₂ O	316	0.201	14.0
KYF ₄	0.1	H ₂ O	1862	0.113	10.0
KYF ₄	0.1	D ₂ O	1862	0.066	15.7

In summary, energy transfer probing was found to be a powerful technique for assessment of the distribution and concentration of energy acceptors inside the material. By means of the energy transfer probe one could also distinguish between a bulk material and nanomaterials.

SUMMARY

The main goal of the thesis was to study the fluorescent properties of the Nd^{3+} doped crystalline nanoparticles, which could be important for biomedical applications, in order to obtain new information about the structural and morphological origins of the fluorescence quenching in the material. The following results were obtained:

- 1) Energy transfer probing, based on a detailed analysis of fluorescence kinetics, allowed us to associate origins of fluorescence quenching with structural and morphological details in rare-earth doped nanomaterials.
- 2) The energy transfer probe allowed us to show that the $-\text{OH}$ acceptor space in the case of the fluorescent inverse opal structures, based on (Tb, Y) chelate complexes with 2-pyrazinecarboxylic acid, is 2-dimensional, so the acceptors are distributed on the surface of the voids of the silica opal template. For the powder of the same phosphor the $-\text{OH}$ acceptor space is measured to be 3-dimensional.
- 3) It was shown experimentally for the first time that for the powder of the Tb^{3+} complexes with 2-pyrazinecarboxylic acid the kinetics of fluorescence quenching accelerated by hopping energy migration ends with the fluctuation stage, which is Förster-like, but has a higher decrement than the static stage. In this case the fluctuation stage starts immediately after static quenching, which is related to an extremely high concentration of $-\text{OH}$ acceptors.
- 4) The study of the quenching kinetics of the $\text{Nd}^{3+}:\text{YPO}_4$ and $\text{Nd}^{3+}:\text{KYF}_4$ nanoparticles revealed that fluorescence quenching is mainly caused by $-\text{OH}$ vibrations (similarly to the case of rare-earth doped glasses). Furthermore, it was shown for $\text{Nd}^{3+}:\text{YPO}_4$ and $\text{Nd}^{3+}:\text{KYF}_4$ nanoparticles that in the case of the low dopant concentration (0.1%) the fluorescence kinetics is determined by static quenching. In the case of the higher concentration (1%) the fluctuation stage immediately follows static quenching. The analysis of the fluctuation stage of the kinetics of hopping quenching allowed us to calculate the ratio between the concentration of acceptors other than donors and the concentration of donors. Comparing the $\text{Nd}^{3+}:\text{YPO}_4$ and $\text{Nd}^{3+}:\text{KYF}_4$ nanoparticles with the same dopant concentration, we found that the concentration of $-\text{OH}$ acceptors is higher in the phosphate nanoparticles.
- 5) By means of the energy transfer probe it was shown that the $-\text{OH}$ acceptor distribution is volumetric in the $\text{Nd}^{3+}:\text{YPO}_4$ and $\text{Nd}^{3+}:\text{KYF}_4$ nanoparticles, so it was concluded that the acceptors are distributed in the mesopores of the material in the form of H_2O molecules and $-\text{OH}$ groups bound to the mesopore surface. In $\text{Nd}^{3+}:\text{YPO}_4$ with the low dopant concentration also the second type of acceptors was detected from the analysis of initial ordered stage of static quenching, implying that the $-\text{OH}$ acceptors are also present in the nearest coordination sphere of the Nd^{3+} donor ion. They were associated with protonated PO_4 groups. The results of energy transfer

probing are fully consistent with the thermal analysis data, which imply that the H₂O molecules and –OH groups bound to the outer surface of the nanoparticles are mostly removed in the course of the thermal treatment, which precedes fluorescence measurements.

- 6) Obtaining well-dispersible 30-40 nm Nd³⁺:KYF₄ nanoparticles, which form suspensions of individual particles allowed us to detect for the first time the slowing down of the fluorescence quenching kinetics at the latest stage due to the restricted geometry of the particles.

SUMMARY IN ESTONIAN

Energiaülekanandesond kui vahend morfoloogiast ja struktuurist tingitud fluoretsentsi kustutamise uurimiseks haruldaste muldmetallidega dopeeritud nanoluminofoorides

Käesoleva doktoritöö põhieesmärgiks oli biomeditsiinilisteks rakendusteks oluliste Nd^{3+} lisandiga dopeeritud anorgaaniliste, kristalliliste nanoosakeste fluoretsentsomaduste uurimine, omandamaks uut teavet fluoretsentsi kustutamise struktuursete ja morfoloogiliste põhjuste kohta seda laadi materjalides. Saadi järgmised tulemused:

- 1) Energiaülekanandesondi meetod, mis põhineb fluoretsentsi kineetika detailsel analüüsil, võimaldas haruldaste muldmetallidega dopeeritud nanomaterjalides tuvastada seose struktuursete ja morfoloogiliste iseärasuste ning fluoretsentsi kustutamise põhjuste vahel.
- 2) Energiaülekanandesondi meetod võimaldas meil näidata, et pööratud opaalstruktuurides, mis põhinevad (Tb, Y) kelaadi kompleksil pürasiin-2-karboksüülhappega, on $-\text{OH}$ aktseptorite ruum kahemõõtmeline, nii et aktseptorid on jaotunud SiO_2 opaalmatriitsi tühemike pinnale. Sama luminofoori pulbris on $-\text{OH}$ aktseptorite ruum kolmemõõtmeline.
- 3) Eksperimentaalselt näidati esmakordselt pürasiin-2-karboksüülhappega seotud Tb^{3+} komplekside jaoks, et hüpleva energiamigratsiooniga kiirendatud fluoretsentsi kustutamise kineetika lõpeb fluktuatsioonilise staadiumiga, mis sarnaneb Försteri protsessile, kuid kustutamise kiirus on suurem võrreldes staatilise kustutamisega. Antud juhul fluktuatsiooniline staadium algab vahetult peale staatilise kustutamise etappi, mis on seotud $-\text{OH}$ aktseptorite erakordselt kõrge kontsentratsiooniga.
- 4) $\text{Nd}^{3+}:\text{YPO}_4$ ja $\text{Nd}^{3+}:\text{KYF}_4$ nanoosakeste fluoretsentsi kustutamise kineetika uurimine näitas, et kustutamist põhjustavad peamiselt $-\text{OH}$ võnkumised (nii nagu haruldaste muldmetallidega dopeeritud klaasides). Esiteks näidati, et dopandi madala kontsentratsiooni puhul (0.1%) on fluoretsentsi kineetika määratud staatilise kustutamisega. Seevastu kõrgema kontsentratsiooni puhul (1%) järgneb staatilisele kustutamisele vahetult fluktuatsiooniline staadium. Hüpleva kustutamise fluktuatsioonilise etapi analüüsimine võimaldas arvutada aktseptorite (v.a. doonorid ise) ja doonorite kontsentratsioonide suhte. Ühesuguse lisandikontsentratsiooniga $\text{Nd}^{3+}:\text{YPO}_4$ ja $\text{Nd}^{3+}:\text{KYF}_4$ nanoosakeste võrdlus näitas, et $-\text{OH}$ aktseptorite kontsentratsioon on kõrgem fosfaatides.
- 5) Energiaülekanandel põhineva sondeerimise kaudu näidati, et $-\text{OH}$ aktseptorite jaotus $\text{Nd}^{3+}:\text{YPO}_4$ ja $\text{Nd}^{3+}:\text{KYF}_4$ nanoosakestes on ruumiline. Seetõttu eeldati, et aktseptorid on jaotunud materjali mesopooridesse H_2O molekulidena ja $-\text{OH}$ rühmadena, mis kinnituvad mesopooride seintele. Staatilise kustutamise korrastatud etapi analüüsil detekteeriti madala lisandikontsentratsiooniga $\text{Nd}^{3+}:\text{YPO}_4$ nanoosakestes lisaks ka teist tüüpi aktseptoreid, mis näitab, et $-\text{OH}$ aktseptorid võivad olla

paigutunud ka Nd^{3+} doonor-iooni lähimasse koordinatsioonisfääri. Seda seostati fosfaatrihma protoneerumisega. Kirjeldatud tulemused on täielikus kooskõlas termogravimeetria andmetega, mis näitasid, et nanoosakeste välispinnale adsorbeerunud vee molekulid ja $-\text{OH}$ rühmad on enamuses eemaldatud fluorestsentsmõõtmistele eelneva termilise töötusega.

- 6) Õnnestus sünteesida 30–40 nm suurusega hästi dispergeeruvad $\text{Nd}^{3+}:\text{KYF}_4$ nanoosakesed, mille kolloidlahuse fluorestsentsi mõõtmine võimaldas esmakordselt detekteerida fluorestsentsi kustutamise kineetika aeglustumist selle hiliseimas staadiumis tingituna osakeste piiratud geometriast.

ACKNOWLEDGEMENTS

I am very grateful to my supervisors Yu.V. Orlovskii and V. Kiisk for their constant support and guidance, to I. Sildos, A.S. Vanetsev, A.V. Popov and S.G. Fedorenko for their assistance and support, and to everyone else who contributed to this work, especially K. Keevend, L. Puust, K. Kaldvee, K. Utt, U. Joost, A.V. Ryabova, V.B. Loschenov, N.A. Glushkov, A.E. Baranchikov, O.K. Alimov, S.O. Klimonsky, S.V. Eliseeva.

I am thankful to my family and friends for their support and understanding.

I acknowledge the European Social Fund (grants MTT050, MJD167, FP7-PEOPLE-2013-IRSES 612620), the Estonian Ministry of Education and Research (Project IUT2-24) and the Estonian Centre of Excellence in Research (Research Project TK114 “Mesosystems: Theory and Applications”) for financial support.

EXTRA

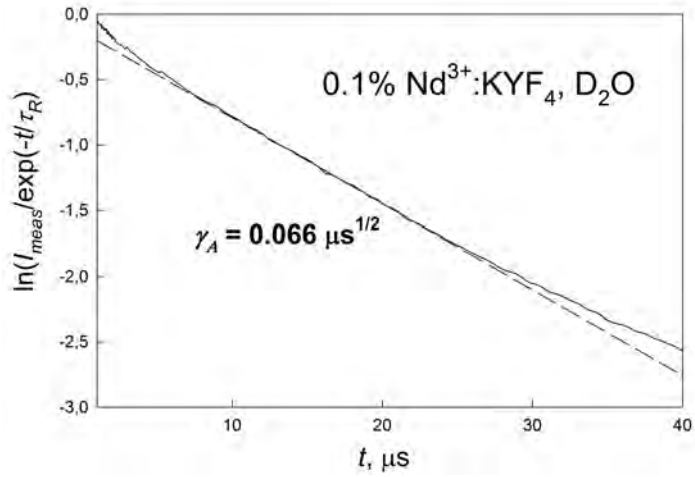


Fig. 32. The disordered stage of the impurity quenching kinetics for the deuterated colloid of the 0.1 at.% $\text{Nd}^{3+}:\text{KYF}_4$ nanoparticles. The dashed curve is the fitting by Eqs. (4, 6).

REFERENCES

1. J. R. DiMaio, B. Kokuoz, J. Ballato. White light emissions through down-conversion of rare-earth doped LaF₃ nanoparticles, *Opt. Express* 14, 23 (2006) 11412–11417.
2. J. W. Stouwdam, G. A. Hebbink, J. Huskens, F. C. J. M. van Veggel. Lanthanide-doped nanoparticles with excellent luminescent properties in organic media, *Chem. Mater.*, 15, 24 (2003) 4604–4616.
3. R. Naccache, F. Vetrone, J. A. Capobianco. Lanthanide-doped upconverting nanoparticles: harvesting light for solar cells, *ChemSusChem* 6 (2013) 1308–1311.
4. M. Darbandi, W. Hoheisel, T. Nann. Silica coated, water dispersible and photoluminescent Y(V,P)O₄:Eu³⁺, Bi³⁺ nanophosphors, *Nanotechnology* 17 (2006) 4168–4173.
5. W. Di, X. Wang, X. Ren. Fluorescent sensing of colloidal CePO₄: Tb nanorods for rapid, ultrasensitive and selective detection of vitamin C, *Nanotechnology* 21 (2010) 365501.
6. M. Wang, C.-C. Mi, W.-X. Wang, C.-H. Liu, Y.-F. Wu, Zh.-R. Xu, Ch.-B. Mao, Sh.-K. Xu. Immunolabeling and NIR-excited fluorescent imaging of HeLa Cells by Using NaYF₄:Yb, Er Upconversion Nanoparticles, *ACS Nano* 3, 6 (2009) 1580–1586.
7. L.-Q. Xiong, Zh.-G. Chen, M.-X. Yu, Fu-You Li, Ch. Liu, Ch.-H. Huang. Synthesis, characterization, and in vivo targeted imaging of amine-functionalized rare-earth up-converting nanophosphors, *Biomaterials* 30, 29 (2009) 5592–5600.
8. F. Vetrone, R. Naccache, A. J. de la Fuente, F. Sanz-Rodríguez, A. Blazquez-Castro, E. Martínez Rodríguez, D. Jaque, J. García Solé, J. A. Capobianco. Intracellular imaging of HeLa cells by non-functionalized NaYF₄:Er³⁺, Yb³⁺ upconverting nanoparticles, *Nanoscale* 2 (2010) 495–498.
9. N.-N. Dong, M. Pedroni, F. Piccinelli, G. Conti, A. Sbarbati, J. E. Ramirez-Hernandez, L. Martínez Maestro, M. C. Iglesias-de la Cruz, F. Sanz-Rodríguez, A. Juarranz, F. Chen, F. Vetrone, J. A. Capobianco, J. García Solé, M. Bettinelli, D. Jaque, A. Speghini. NIR-to-NIR two-photon excited CaF₂: Tm³⁺, Yb³⁺ nanoparticles: multifunctional nanoprobe for highly penetrating fluorescence bioimaging, *ACS Nano* 5, 11 (2011) 8665–8671.
10. D. P. Dutta, R. S. Ningthoujam, A. K. Tyagi. Luminescence properties of Sm³⁺ doped YPO₄: effect of solvent, heat-treatment, Ca²⁺/W⁶⁺-co-doping and its hyperthermia application. *AIP Adv.* 2 (2012) 042184.
11. U. Rocha, K. U. Kumar, C. Jacinto, I. Villa, F. Sanz-Rodríguez, M. Del Carmen Iglesias De La Cruz, A. Juarranz, E. Carrasco, F. C. J. M. Van Veggel, E. Bovero, J. García Solé, D. Jaque. Neodymium-doped LaF₃ nanoparticles for fluorescence bioimaging in the second biological window, *Small* 10 (2014) 1141–1154.
12. D. Jaque, L. Martínez Maestro, B. del Rosal, P. Haro-Gonzalez, A. Benayas, J. L. Plaza, E. Martín Rodríguez, J. García Solé. Nanoparticles for photothermal therapies, *Nanoscale* 6 (2014) 9494–9530.
13. A. M. Smith, M. C. Mancini, S. Nie. Bioimaging: second window for in vivo imaging, *Nat. Nanotechnol.* 4, 11 (2009) 710–711.
14. G. L. Prasad. Biomedical Applications of Nanoparticles, in: *Safety of Nanoparticles (From Manufacturing to Medical Applications)*, Ed. Thomas J. Webster, Springer, 2009, 89–109.

15. A. Gnach, T. Lipinski, A. Bednarkiewicz, J. Rybka, J. A. Capobianco. Upconverting nanoparticles: assessing the toxicity, *Chem. Soc. Rev.* 44 (2015) 1561–1584.
16. M. Longmire, P. L. Choyke, H. Kobayashi. Clearance properties of nano-sized particles and molecules as imaging agents: considerations and caveats, *Nano-medicine* 3, 5 (2008) 703–717.
17. D. M. Smith, J. K. Simon, J. R. Baker Jr. Applications of nanotechnology for immunology, *Nat. Rev. Immunol.* 13 (2013) 592–605.
18. A. Gnach, A. Bednarkiewicz. Lanthanide-doped up-converting nanoparticles: Merits and challenges, *NanoToday* 7, 6 (2012) 532–563.
19. S. Polizzi, G. Fagherazzi, M. Battagliarin, M. Bettinelli, A. Speghini. Fractal aggregates of lanthanide-doped Y_2O_3 nanoparticles obtained by propellant synthesis, *J. Mater. Res.* 16, 1 (2001) 146–154.
20. R. L. Axelbaum, D. P. DuFaux, and C. A. Frey, K. F. Kelton, S. A. Lawton, L. J. Rosen, S. M. L. Sastry. Synthesis and optical properties of nanosized powders: lanthanide-doped Y_2O_3 , *Appl. Surf. Sci.* 144–145 (1999) 686–689.
21. J. A. Capobianco, J. C. Boyer, F. Vetrone, A. Speghini, M. Bettinelli. Optical spectroscopy and upconversion studies of Ho^{3+} -doped bulk and nanocrystalline Y_2O_3 , *Chem. Mater.* 14 (2002) 2915–2921.
22. F. Vetrone, J. C. Boyer, J. A. Capobianco, A. Speghini, M. Bettinelli. Effect of Yb^{3+} codoping on the upconversion emission in nanocrystalline $\text{Y}_2\text{O}_3:\text{Er}^{3+}$, *J. Phys. Chem. B* 107, 5 (2003) 1107–1112.
23. F. Vetrone, J. C. Boyer, J. A. Capobianco, A. Speghini, M. Bettinelli. Significance of Yb^{3+} concentration on the upconversion mechanisms in codoped $\text{Y}_2\text{O}_3:\text{Er}^{3+}$, Yb^{3+} nanocrystals, *J. Appl. Phys.* 96, 1 (2004) 660–667.
24. H. Eilers, B. M. Tissue. Laser spectroscopy of nanocrystalline Eu_2O_3 , and $\text{Eu}^{3+}:\text{Y}_2\text{O}_3$, *Chem. Phys. Lett.* 251 (1996) 74–78.
25. V. V. Osipov, Yu. A. Kotov, M. G. Ivanov, O. M. Samatov, V. V. Lisenkov, V. V. Platonov, A. M. Murzakaev, A. I. Medvedev, E. I. Azarkevich. Laser synthesis of nanopowders, *Las. Phys.* 16, 1 (2006) 116–125.
26. J. C. Boyer, F. Vetrone, L. A. Cuccia, J. A. Capobianco. Synthesis of colloidal upconverting NaYF_4 nanocrystals doped with Er^{3+} , Yb^{3+} and Tm^{3+} , Yb^{3+} via thermal decomposition of lanthanide trifluoroacetate precursors, *J. Am. Chem. Soc.* 128 (2006) 7444–7445.
27. C. Li, J. Lin. Rare earth fluoride nano-/microcrystals: synthesis, surface modification and application, *J. Mater. Chem.* 20 (2010) 6831–6847.
28. F. Vetrone, R. Naccache, V. Mahalingam, C. G. Morgan, J. A. Capobianco. The active-core/active-shell approach: a strategy to enhance the upconversion luminescence in lanthanide-doped nanoparticles, *Adv. Funct. Mater.* 19 (2009) 2924–2929.
29. N. J. J. Johnson, N. M. Sangeetha, J. C. Boyer, F. C. J. M. van Veggel. Facile ligand-exchange with polyvinylpyrrolidone and subsequent silica coating of hydrophobic upconverting $\beta\text{-NaYF}_4:\text{Yb}^{3+}/\text{Er}^{3+}$ nanoparticles, *Nanoscale* 2 (2010) 771–777.
30. S. J. Budijono, J. Shan, N. Yao, Yu. Miura, Th. Hoye, R. H. Austin, Y. Ju, R. K. Prudhomme. Synthesis of stable block-copolymer-protected $\text{NaYF}_4:\text{Yb}^{3+},\text{Er}^{3+}$ up-converting phosphor nanoparticles, *Chem. Mater.* 22 (2010) 311–318.
31. N. Bogdan, F. Vetrone, G. A. Ozin, J. A. Capobianco. Synthesis of ligand-free colloiddally stable water dispersible brightly luminescent lanthanide-doped upconverting nanoparticles, *Nano Lett.* 11 (2011) 835–840.

32. R. A. Jalil, Y. Zhang. Biocompatibility of silica coated NaYF₄ upconversion fluorescent nanocrystals, *Biomaterials* 29, 30 (2008) 4122–4128.
33. Y. Wei, F. Lu, X. Zhang, D. Chen. Polyol-mediated synthesis and luminescence of lanthanide-doped NaYF₄ nanocrystal upconversion phosphors, *J. All. Comp.* 455 (2008) 376–384.
34. Z. Li, Y. Zhang. Monodisperse silica-coated polyvinylpyrrolidone/NaYF₄ nanocrystals with multicolor upconversion fluorescence emission, *Angew. Chem. Int. Ed.* 45 (2006) 7732–7735.
35. Sh. Gai, Ch. Li, P. Yang, J. Lin. Recent progress in rare earth micro/nanocrystals: soft chemical synthesis, luminescent properties, and biomedical applications, *Chem. Rev.* 114 (2014) 2343–2389.
36. J.-L. Lemyre, A. M. Ritcey. Synthesis of lanthanide fluoride nanoparticles of varying shape and size, *Chem. Mater.* 17, 11 (2005) 3040–3043.
37. P. Li, Q. Peng, Y. Li. Dual-mode luminescent colloidal spheres from monodisperse rare-earth fluoride nanocrystals, *Adv. Mater.* 21 (2009) 1945–1948.
38. H. Lai, A. Bao, Y. Yang, Y. Tao, H. Yang, Y. Zhang, L. Han. UV luminescence property of YPO₄:RE (RE = Ce³⁺, Tb³⁺), *J. Phys. Chem. C* 112 (2008) 282–286.
39. W.-S. Song, Y.-S. Kim, H. Yang. Hydrothermal synthesis of self-emitting Y(V,P)O₄ nanophosphors for fabrication of transparent blue-emitting display device, *J. Lumin.* 132 (2012) 1278–1284.
40. A. S. Vanetsev, O. M. Gaitko, I. G. Chuvashova, M. N. Sokolov, Yu. D. Tretyakov. Microwave hydrothermal synthesis of nanodispersed YV_{1-x}P_xO₄:Eu powders, *Doklady Chem.* 441 (2011) 325–329.
41. T. Holstein, S. K. Lyo, R. Orbach. Excitation transfer in disordered systems, in: *Laser Spectroscopy of Solids*, Eds: W. M. Yen, P. M. Selzer, Springer, 1986, Vol. 49, 39–82.
42. Th. von Förster. Zwischenmolekulare Energiewanderung und Fluoreszenz, *Ann. Phys.* 2 (1948) 55–75.
43. V. P. Sakun. Kinetics of energy transfer in a crystal, *Sov. Phys. Solid State* 14 (1972) 1906–1914.
44. A. G. Avanesov, T. T. Basiev, Yu. K. Voron'ko, B. I. Denker, A. Ya. Karasik, G. V. Maksimova, V. V. Osiko, V. F. Pisarenko, A. M. Prokhorov. Neodymium electron energy deactivation and transfer in highly concentrated phosphate glasses, *Sov. Phys. JETP* 50 (1979) 886–895.
45. L. Stryer. Fluorescence energy transfer as a spectroscopic ruler, *Ann. Rev. Biochem.* 47 (1978) 819–846.
46. P. Levitz, J. M. Drake, J. Klafter. Critical evaluation of the application of direct energy transfer in probing the morphology of porous solids, *J. Chem. Phys.* 89, 8 (1988) 5224–5236.
47. A. I. Burshtein, A. B. Doktorov, A. A. Kipriyanov, V. A. Morozov, S. G. Fedorenko. Regions of applicability of kinematic mechanisms in bimolecular processes, *JETP* 61, 3 (1985) 516–521.
48. A. I. Burshtein. Concentration quenching of incoherent excitations in solutions, *Sov. Phys. Usp.* 143, 4 (1984) 553–600.
49. S. G. Fedorenko, A. I. Burshtein, A. A. Kipriyanov. Fluctuation asymptotics of hopping quenching in disordered systems, *Phys. Rev. B* 48 (1993) 7020–7029.
50. Yu. V. Orlovskii, A. V. Popov, V. V. Platonov, S. G. Fedorenko, I. Sildos, V. V. Osipov. Fluctuation kinetics of fluorescence hopping quenching in the Nd³⁺:Y₂O₃ spherical nanoparticles, *J. Lumin.* 139 (2013) 91–97.

51. A. V. Popov, Yu. V. Orlovskii, A. S. Vanetsev, O. M. Gaitko, E. O. Orlovskaya, I. Sildos. Nanosecond fluctuation kinetics of luminescence hopping quenching originated from the $5d^1$ level in the $Ce^{3+}:YPO_4 \cdot 0.8H_2O$ nanocrystals, *J. Lumin.* 145 (2014) 774–778.
52. S. G. Fedorenko, A. I. Burshtein. Binary Theory of Impurity Quenching Accelerated by Resonant Excitation Migration in a Disordered System, *Chem. Phys.* 128 (1988) 185–198.
53. S. V. Eliseeva, O. V. Mirzov, S. I. Troyanov, A. G. Vitukhnovsky, N. P. Kuzmina. Synthesis, characterization and luminescence properties of europium(III) and terbium(III) complexes with 2-pyrazinecarboxylic acid: Crystal structure of $[Eu(pyca)_3(H_2O)_2] \cdot 6H_2O$, *J. All. Comp.* 374, 1–2 (2004) 293–297.
54. J. W. Goodwin, J. Hearn, C. C. Ho, R. H. Ottewill. Studies on the preparation and characterisation of monodisperse polystyrene latices, *Colloid Polym. Sci.* 252 (1974) 464–471.
55. A. S. Sinitskii, P. E. Khokhlov, V. V. Abramova, T. V. Laptinskaya, Yu. D. Tretyakov. Optical study of photonic crystal films made of polystyrene microspheres, *Mend. Comm.* 17, 1 (2007) 4–6.
56. P. E. Khokhlov, A. S. Sinitskii, Yu. D. Tretyakov. Inverse photonic crystals based on silica, *Doklady Chem.* 408, 1 (2006) 61–64.
57. M. Li, P. Zhang, J. Li, J. Zhou, A. Sinitskii, V. Abramova, S. O. Klimonsky, Yu. D. Tretyakov. Directional emission from rare earth ions in inverse photonic crystals, *Appl. Phys. B* 89, 2-3 (2007) 251–255.
58. H. Schäfer, P. Ptacek, O. Zerzouf, M. Haase. Synthesis and optical properties of $KYF_4/Yb, Er$ nanocrystals, and their surface modification with undoped KYF_4 , *Adv. Funct. Mater.* 18 (2008) 2913–2918.
59. Y. Wang, Y. Liu, Q. Xiao, H. Zhu, R. Li, X. Chen. Eu^{3+} doped KYF_4 nanocrystals: synthesis, electronic structure, and optical properties, *Nanoscale* 3 (2011) 3164–3169.
60. W. T. Carnall, H. Crosswhite, H. M. Crosswhite. Energy level structure and transition probabilities of the trivalent lanthanides in LaF_3 , *Internal Report of Argonne National Laboratory*, Argonne, Illinois (1975).
61. R. T. Downs, M. Hall-Wallace. The American Mineralogist Crystal Structure Database. *Amer. Mineral.* 88 (2003) 247–250.
62. Yu. Ni, J. M. Hughes, A. N. Mariano. Crystal chemistry of the monazite and xenotime structures, *Amer. Mineral.* 80 (1995) 21–26.
63. R. P. Denkwicz, Jr., K. S. TenHuisen, J. H. Adair. Hydrothermal crystallization kinetics of m-ZrQ₂ and t-ZrQ₂, *J. Mater. Res.* 5, 11 (1990) 2698–2705.
64. Q. Chang, J. Zhou, Y. Wang, G. Meng. Formation mechanism of zirconia nanoparticles containing pores prepared via sol–gel-hydrothermal method, *Adv. Powder Technol.* 21 (2010) 425–430.
65. O. K. Alimov, T. T. Basiev, M. K. Ashurov, E. O. Kirpichenkova, V. B. Murav'ev. Electron-excitation energy transfer among impurity ions in disordered media, in: *Selective laser spectroscopy of activated crystals and glasses*, Ed.: V. V. Osiko, *Proceedings of GPI - 9*, Nova Science Publishers, New York, 1990, 67–203.
66. W. O. Milligan, D. F. Mullica, G. W. Beall, L. A. Boatner. Structural investigations of YPO_4 , $ScPO_4$, and $LuPO_4$, *Inorg. Chim. Acta* 60 (1982) 39–43.
67. O. Guillot-Noel, B. Viana, B. Bellamy, D. Gourier, G. B. Zogo-Mboulou, S. Jandl. Spectroscopic evidence of inhomogeneous distribution of Nd^{3+} in YVO_4 , YPO_4 , and $YAsO_4$ Crystals, *Opt. Mat.* 13 (2000) 427–437.

68. T. T. Basiev, Yu. V. Orlovskii. Nonradiative energy transfer from high-lying highly-quenched multiplets of Nd^{3+} in the LaF_3 laser crystal, *Sov. Phys. JETP* 69, 6 (1989) 1109–1118.
69. N. A. Glushkov, T. T. Basiev, Yu. V. and Orlovskii. Kinetics of the direct quenching of optical excitation in crystalline nanoparticles, *Nanotechnol. Russ.* 4 (2009) 722–731.
70. D. L. Dexter. A theory of sensitized luminescence in solids, *J. Chem. Phys.* 21 (1953) 836–850.
71. V. M. Agranovich, M. D. Galanin. Electron Excitation Energy Transfer in Condensed Matter Series: Modern Problems in Condensed Matter Sciences, Elsevier North-Holland in Amsterdam, New York, 1982, Vol. 3.

CURRICULUM VITAE

Name: Elena Samsonova
Date of birth: 29.11.1988
Nationality: Russian
Phone number: +37258437074
E-mail: elena.samsonova@ut.ee
Occupation: Laboratory assistant, University of Tartu, Institute of Physics, Tartu, Estonia

Education:

2011 M.Sc., Lomonosov Moscow State University, Department of Materials Science, Moscow, Russia.
2009 B.Sc., Lomonosov Moscow State University, Department of Materials Science, Moscow, Russia.
2005 Gymnasium 1, Penza, Russia.

Languages: Russian (native), English (fluent), German (basic).

Career:

2013–2015 Laboratory assistant, Laboratory assistant, University of Tartu, Institute of Physics, Tartu, Estonia.
2013–2013 Junior researcher, Institute of General Pathology and Pathophysiology, Moscow, Russia.
2008–2011 Engineer, Prokhorov General Physics Institute, Russian Academy of Sciences, Moscow, Russia.

Publications included in the thesis:

1. Orlovskii, Yu.V.; Basiev, T.T.; Samsonova, E.V.; Glushkov, N.A.; Eliseeva, S.V.; Alimov, O.K.; Orlovskii, A.Yu.; Klimonsky, S.O. Energy Transfer Probe for Characterization of Luminescent Photonic Crystals Morphology. *Journal of Luminescence*, 131(3); 2011, 449–452.

2. Fedorenko, S.G.; Orlovskii, Yu.V., Samsonova, E.V. Fluctuation kinetics of the hopping fluorescence quenching in disordered solid solutions. A theoretical model and experimental evidence. *Journal of Luminescence*, 131(11); 2011, 2409–2413.

3. Samsonova, E.V.; Popov, A.V.; Vanetsev, A.S.; Keevend, K.; Orlovskaya, E.O.; Kiisk, V.; Lange, S.; Joost, U.; Kaldvee, K.; Mäeorg, U.; Glushkov, N.; Ryabova, A. V.; Sildos, I.; Osiko, V.V.; Steiner, R.; Loschenov, V.B.; Orlovskii, Yu. V. An energy transfer kinetic probe for OH-quenchers in the Nd³⁺:YPO₄ nanocrystals suitable for imaging in the biological tissue transparency window. *Physical Chemistry Chemical Physics*, 16(48); 2014, 26806–26815.4. Vanetsev, A.S.; Samsonova, E.V.; Gaitko, O.M.; Keevend, K.;

Popov, A.V.; Mäeorg, U.; Mändar, H.; Sildos, I.; Orlovskii, Yu.V. Phase composition and morphology of nanoparticles of yttrium orthophosphates synthesized by microwave-hydrothermal treatment: the influence of synthetic conditions. *Journal of Alloys and Compounds*, 639; 2015, 415–421.

5. Samsonova, E.V.; Popov, A.V.; Vanetsev, A.S.; Keevend, K.; Kaldvee, K.; Baranchikov, A.E.; Ryabova, A.V.; Fedorenko, S.G.; Sildos, I.; Kikas, J.; Steiner, R.; Loschenov, V.B.; Orlovskii, Y.V. Fluorescence quenching mechanism for water-dispersible $\text{Nd}^{3+}:\text{KYF}_4$ nanoparticles synthesized by microwave-hydrothermal technique. *Journal of Luminescence*; 2015 x–x (in press).

Other publications

1. Komissarova, L.N.; Ryumin, M.A.; Pukhkaya, V.V.; Samsonova, E.V.; Orlovskii, Yu.V. Synthesis and study of the properties of the $\text{K}_2\text{Y}_{1-x-y}\text{Eu}_x\text{Tb}_y(\text{MoO}_4)(\text{PO}_4)$ and $\text{K}_2\text{Y}_{1-x-y}\text{Eu}_x\text{Tb}_y(\text{MoO}_4)(\text{PO}_4)_{1-\delta}(\text{VO}_4)_\delta$ solid solutions. *Russian Journal of Inorganic Chemistry*, 56(12); 2011, 1943–1950.

2. Orlovskii, Yu.V.; Vanetsev, A.S.; Romanishkin, I.D.; Ryabova, A.V.; Pukhov, K.K.; Baranchikov, A.E.; Samsonova, E.V.; Keevend, K.; Sildos, I.; Loschenov, V.B. Laser heating of the $\text{Y}_{1-x}\text{Dy}_x\text{PO}_4$ nanocrystals. *Optical Materials Express*, 5(5); 2015, 1230–1239.

Scholarships

2013 – present PhD scholarship, University of Tartu.
2012–2012 IMPRS-SurMat scholarship, Max-Planck Institute for Coal Research, Mülheim-an-der-Ruhr, Germany.

ELULOOKIRJELDUS

Nimi: Elena Samsonova
Sünniaeg: 29.11.1988
Kodakondsus: Venelane
Telefon: +37258437074
E-post: elena.samsonova@ut.ee
Töökoht, amet: laborant, Tartu Ülikool, Füüsika Instituut, Tartu, Eesti

Haridus:

2011 M.Sc., Lomonossovi nimeline Moskva Riiklik Ülikool, materjaliteaduse osakond, Moskva, Venemaa.
2009 B.Sc., Lomonossovi nimeline Moskva Riiklik Ülikool, materjaliteaduse osakond, Moskva, Venemaa.
2005 Gümnaasium 1, Penza, Venemaa.

Keelteoskus: vene keel (emakeel), inglise keel (kõrgtase), saksa keel (algfase).

Töökogemus:

2013–2015 laborant, Tartu Ülikool, Füüsika Instituut, Tartu, Eesti.
2013–2013 noorteadur, Üldise Patoloogia ja Patofüsioloogia Instituut, Moskva, Venemaa.
2008–2011 inseneer, Prokhorovi nimeline Üldise Füüsika Instituut, Vene Teaduste Akadeemia, Moskva, Venemaa.

Teeside aluseks olevate publikatsioonide loetelu:

1. Orlovskii, Yu.V.; Basiev, T.T.; Samsonova, E.V.; Glushkov, N.A.; Eliseeva, S.V.; Alimov, O.K.; Orlovskii, A.Yu.; Klimonsky, S.O. Energy Transfer Probe for Characterization of Luminescent Photonic Crystals Morphology. *Journal of Luminescence*, 131(3); 2011, 449–452.
2. Fedorenko, S.G.; Orlovskii, Yu.V., Samsonova, E.V. Fluctuation kinetics of the hopping fluorescence quenching in disordered solid solutions. A theoretical model and experimental evidence. *Journal of Luminescence*, 131(11); 2011, 2409–2413.
3. Samsonova, E.V.; Popov, A.V.; Vanetsev, A.S.; Keevend, K.; Orlovskaya, E.O.; Kiisk, V.; Lange, S.; Joost, U.; Kaldvee, K.; Mäeorg, U.; Glushkov, N.; Ryabova, A. V.; Sildos, I.; Osiko, V.V.; Steiner, R.; Loschenov, V.B.; Orlovskii, Yu. V. An energy transfer kinetic probe for OH-quenchers in the Nd³⁺:YPO₄ nanocrystals suitable for imaging in the biological tissue transparency window. *Physical Chemistry Chemical Physics*, 16(48); 2014, 26806–26815.

4. Vanetsev, A.S.; Samsonova, E.V.; Gaitko, O.M.; Keevend, K.; Popov, A.V.; Mäeorg, U.; Mändar, H.; Sildos, I.; Orlovskii, Yu.V. Phase composition and morphology of nanoparticles of yttrium orthophosphates synthesized by microwave-hydrothermal treatment: the influence of synthetic conditions. *Journal of Alloys and Compounds*, 639; 2015, 415–421.

5. Samsonova, E.V.; Popov, A.V.; Vanetsev, A.S.; Keevend, K.; Kaldvee, K.; Baranchikov, A.E.; Ryabova, A.V.; Fedorenko, S.G.; Sildos, I.; Kikas, J.; Steiner, R.; Loschenov, V.B.; Orlovskii, Y.V. Fluorescence quenching mechanism for water-dispersible Nd³⁺:KYF₄ nanoparticles synthesized by microwave- hydrothermal technique. *Journal of Luminescence*; 2015, x–x (in press).

Autori muud publikatsioonid:

1. Komissarova, L.N.; Ryumin, M.A.; Pukhkaya, V.V.; Samsonova, E.V.; Orlovskii, Yu.V. Synthesis and study of the properties of the K₂Y_{1-x-y}Eu_xTb_y(MoO₄)(PO₄) and K₂Y_{1-x-y}Eu_xTb_y(MoO₄)(PO₄)_{1-δ}(VO₄)_δ solid solutions. *Russian Journal of Inorganic Chemistry*, 56(12); 2011, 1943–1950.

2. Orlovskii, Yu.V.; Vanetsev, A.S.; Romanishkin, I.D.; Ryabova, A.V.; Pukhov, K.K.; Baranchikov, A.E.; Samsonova, E.V.; Keevend, K.; Sildos, I.; Loschenov, V.B. Laser heating of the Y_{1-x}Dy_xPO₄ nanocrystals. *Optical Materials Express*, 5(5); 2015, 1230–1239.

Stipendiumid

2013 – praeguseni
2012–2012

doktorandi stipendium, Tartu Ülikool.

IMPRS-SurMat stipendium, Max-Plancki nimeline Kivi-
sõeuuringute Instituut, Mülheim-an-der-Ruhr, Saksamaa.

DISSERTATIONES SCIENTIAE MATERIALIS UNIVERSITATIS TARTUENSIS

1. **Martin Järvekülg.** Tubular microstructures by Hf-, Zr- and Ti-butoxide gel sheet rolling. Tartu, 2011, 112 p.
2. **Sergei Vlassov.** Investigation of nanoscale interactions and mechanical properties of nanostructures using quartz tuning fork based real-time measurements. Tartu, 2011, 171 p.
3. **Margus Kodu.** Pulsed Laser Deposition of Magnesium Oxide and Barium Ternary Oxides for Plasma Display Protective Layers. Tartu, 2011, 89 p.
4. **Rainer Pärna.** Surface studies of some oxide films. Tartu, 2011, 129 p.
5. **Jevgeni Šulga.** Self-assembly and interaction of nanostructures. Tartu, 2011, 114 p.
6. **Wojciech Kuznik.** Quantum-chemical computer simulations of the linear and non-linear optical properties of pyrazoloquinoline and dicyanopyrazine derivatives. Tartu, 2012, 89 p.
7. **Leonid Dorogin.** Structural and tribological properties of zero- and one-dimensional nanocrystals. Tartu, 2012, 193 p.
8. **Viljar Palmre.** Fabrication and characterization of microporous carbon-based electroactive polymer actuators. Tartu, 2012, 99 p.
9. **Madis Paalo.** Synthesis of CNT-metal oxide nanocomposites: sol-gel process, rheology, structural and functional properties. Tartu, 2014, 175 p.
10. **Raul Välbe.** Development of ionic liquid composites by sol-gel method for elaboration of industrial nano- and microstructures. Tartu, 2014, 97 p.
11. **Urmas Joost.** Impurity and preparation dependent properties of titania thin films. Tartu, 2014, 155 p.
12. **Madis Umalas.** Application of sol-gel technology for production of ceramic nanocomposites and functional coatings. Tartu, 2015, 136 p.